Link between crustal thickness and Moho transition zone at 9oN East Pacific Rise

Zhikai Wang[1], Satish Chandra Singh[2], and Juan Pablo Canales[3]

[1]University of Southampton
[2]Institut De Physique Du Globe De Paris
[3]Woods Hole Oceanographic Institution

April 12, 2024

Abstract

Oceanic crust at fast-spreading ridges is formed by melt percolating through the Mohorovičić Transition Zone (MTZ), the boundary between crust and mantle. However, the relationship between the crustal structures and MTZ remains elusive. Applying full waveform inversion to wide-angle seismic data acquired near the 9oN East Pacific Rise, we show that the variations in crustal MTZ thicknesses are inversely correlated along the segment, although their total cumulative thickness shows little variations. These variations could be attributed to different melt migration efficiency through MTZ or variation in mantle thermal structures. Thin MTZ could be due to rapid percolation of melt from mantle to crust whereas the thick MTZ results from the crystallization of melt within the transition zone. On the other hand, for relatively hot segments, melt will accumulate at shallower depth within the lower crust. In contrast, melt could freeze at Moho depth for relatively cold segments thickening the MTZ.

Link between crustal thickness and Moho transition zone at 9ºN East Pacific Rise

Zhikai Wang[1,2], Satish C. Singh[1], and J. Pablo Canales[3]

[1] Institut de Physique du Globe de Paris, Université Paris Cité, 1 Rue Jussieu, 75005 Paris, France.

[2] Presently at School of Ocean and Earth Science, University of Southampton, European Way, SO14 3ZH Southampton, UK.

[3] Department of Geology and Geophysics, Woods Hole Oceanographic Institution, Woods Hole MA 02543, USA.

Abstract

Oceanic crust at fast-spreading ridges is formed by melt percolating through the Mohorovičić Transition Zone (MTZ), the boundary between crust and mantle. However, the relationship between the crustal structures and MTZ remains elusive. Applying full waveform inversion to wide-angle seismic data acquired near the 9ºN East Pacific Rise, we show that the variations in crustal MTZ thicknesses are inversely correlated along the segment, although their total cumulative thickness shows little variations. These variations could be attributed to different melt migration efficiency through MTZ or variation in mantle thermal structures. Thin MTZ could be due to rapid percolation of melt from mantle to crust whereas the thick MTZ results from the crystallization of melt within the transition zone. On the other hand, for relatively hot segments, melt will accumulate at shallower depth within the lower crust. In contrast, melt could freeze at Moho depth for relatively cold segments thickening the MTZ.

Plain Language Summary

At the spreading centres where two plates move apart, the basaltic melt produced by decompression melting of the upwelling mantle forms new oceanic crust. The oceanic crust is separated from the underlying mantle by the Mohorovičić Transition Zone (MTZ). However, the relationship between the crustal structures and MTZ is poorly known. We applied seismic full waveform inversion, a state-of-the-art seismic imaging method, to the wide-angle seismic data collected from a young oceanic crust near the 9°N East Pacific Rise. We found that the crustal thickness varies from 5.1 to 6.5 km along a 70 km-long crustal segment. Interestingly, the MTZ thickness varies between 1.1 to 2.4 km along the segment and is inversely correlated with crustal thickness. The total cumulative thickness of crust and MTZ keeps almost constant along the profile. These variations could be explained either by different melt migration efficiency through MTZ or by changes in mantle thermal structures along the ridge segment.

Key points:

- We apply elastic-wave full waveform inversion to wide-angle seismic data acquired near the 9°N East Pacific Rise
- The high-resolution crustal velocity model shows that the crustal thickness varies between 5.1 and 6.5 km along a 70 km-long crustal segment
- The thickness of Moho transition zone is inversely correlated with crustal thickness along the segment

1. Introduction

Oceanic crust is formed at mid-ocean ridges (MORs) from basaltic melt derived from decompression of upwelling mantle as two lithospheric plates move apart (Cann, 1970). In a fast and intermediate-spreading environment, the melt rises towards the surface and accumulates within an axial magma chamber (AMC) at mid-crustal depths (Detrick *et al.*, 1987; Mutter *et al.*, 1988). A portion of the accumulated melt erupts to form lava flows on the seafloor and dike underneath, making up the upper crust. The remainder of the melt crystallises within the AMC, forming the gabbroic lower crust. The crust is separated from the underlying mantle by the Moho Transition Zone (MTZ). Determining the relationship between the oceanic crustal structure and the MTZ is critical for understanding the crustal accretion at MORs.

Traveltime tomography of wide-angle seismic refraction data has revealed that the magmatic crust consists of two layers: an upper crust characterised by low P-wave velocities (Vp: 3.0-6.5 km/s) but high velocity gradients and a lower crust exhibiting high Vp (6.5-7.1 km/s) and significantly reduced velocity gradient (Christeson *et al.*, 2019; White *et al.*, 1992). The mantle underneath has a Vp >7.7 km/s and consists primarily of peridotite (Christeson *et al.*, 2019; Wang and Singh, 2022). However, traveltime tomography constrains the lower crustal velocity using wide-angle reflections (PmP) from the Moho, resulting in a trade-off between the lower crustal velocity and the Moho depth (Vaddineni *et al.*, 2021). Furthermore, the Moho is commonly assumed to be a sharp interface in traveltime tomography (Canales *et al.*, 2003; Vaddineni *et al.*, 2021; Wang and Singh, 2022), which has precluded determining the relationship between the crustal structure and the MTZ.

Multi-channel seismic (MCS) data provide reflection images of the oceanic Moho formed at fast- and intermediate-spreading ridges with seismic characters ranging from impulsive, shingled and diffusive (Aghaei *et al.*, 2014; Kent *et al.*, 1994). The impulsive and shingled Moho are characterized by a single-phase reflection while the diffusive Moho shows sub-horizontally multi-phase reflection events (Aghaei *et al.*, 2014; Barth and Mutter, 1996; Kent *et al.*, 1994). Seismic waveform modelling demonstrates that the impulsive and shingled Moho reflections are probably produced by a thin MTZ and the diffusive Moho indicates a relatively thick MTZ (Brocher *et al.*, 1985; Collins *et al.*, 1986). Nedimović *et al.* (2005) suggest that the multi-phase Moho reflection events might be caused by the frozen magma lenses within a thick MTZ. However, MCS data provide the Moho structure in two-way traveltime, which needs to be converted to depth. Due to the lack of accurate velocity model of the subsurface, the uncertainty in the inferred Moho depth can be hundreds metres (Aghaei *et al.*, 2014; Barth and Mutter, 1996), and even >1 km in some cases (Barth and Mutter, 1996). Therefore, our understanding of MTZ from seismic methods remain elusive.

Structural mapping of ophiolites, which are thought to be formed at ancient spreading ridges, indicates that the MTZ is primarily composed of dunites with gabbroic sills and lenses, marking a gradually downward change from layered gabbro in the lower crust to ultramafic mantle consisting dominantly of harzburgites (Benn *et al.*, 1988; Boudier and Nicolas, 1995; Karson *et al.*, 1984). The thickness of the MTZ varies from 5-10 m to 1-3 km (Benn *et al.*, 1988; Karson *et al.*, 1984), where the thickness of gabbroic sills and lenses can reach hundreds of meters in a thick MTZ (Benn *et al.*, 1988; Boudier and Nicolas, 1995; Karson *et al.*, 1984). The strong magmatic flow structures within the MTZ indicate that these gabbroic sills were emplaced at the ridge axis, implying that a large amount of melt was trapped within the MTZ during crustal accretion (Boudier and Nicolas, 1995). However, in the absence of drilling results, we do not have any in situ information about the MTZ.

Here, we present results of the application of two-dimensional (2-D) elastic full waveform inversion (FWI) (Shipp and Singh, 2002) to wide-angle seismic data to constrain the Vp of the crust and MTZ of young oceanic crust near the East Pacific Rise (EPR) at 9°-10°N. FWI can provide high-resolution velocity model of the subsurface at a vertical resolution of half a wavelength (Virieux and Operto, 2009), i.e. hundreds meter (Guo *et al.*, 2022; Jian *et al.*, 2021), important for studying the fine-scale structures of oceanic crust and MTZ.

2. Seismic data and full waveform inversion

The seismic data were acquired from the fast-spreading (11 cm/yr) EPR between 8°15'N and 10°05'N during the 1997 Undershoot Seismic Experiment (Toomey *et al.*, 1997). Although the undershoot experiment was performed covering the whole 9°N EPR segment on both flanks (Toomey *et al.*, 1997), here we use only six ocean bottom instruments deployed at dominantly ~8-14 km intervals along a 92 km-long profile on the eastern flank of the EPR (Figure 1) between the Clipperton transform fault (TF; first-order discontinuity) and the 9°03'N overlapping spreading centre (OSC; second-order discontinuity). The EPR between the 9°03'N OSC and the Clipperton TF is further offset by the third-order discontinuities at 9°12'N, 9°20'N, 9°37'N, 9°51.5'N and 9°58'N, respectively (black rectangles in Figure 1; (Aghaei *et al.*, 2014; White *et al.*, 2006)). The source was an airgun array with a total volume of 8503 in^3, towed at 10 m depth and fired at ~ 460 m interval.

We simultaneously inverted the pressure data recorded by ocean bottom hydrophones (OBHs) and the vertical component data of ocean bottom seismometers (OBSs). We band-pass filtered the data between 3 and 30 Hz and applied a predictive gapped deconvolution with minimum and maximum lags of 0.14 s and 0.35 s to suppress the seismic bubbles (Figure S1). The deconvolved data were transformed from three-dimensional (3-D) to 2-D by multiplying the amplitude of the data by $\sqrt{t}$ (where t is the traveltime) and convolving the seismic data with $1/\sqrt{t}$ (Pica *et al.*, 1990). A 1.0 s-wide time windowing was applied to extract the Pg, PmP and mantle refraction (Pn) arrivals between 6 and 60 km offsets (Figure S2). The top of the time window is 0.1 s prior the picked first arrival traveltime. In this work, we inverted the seismic data of two frequency bands, first 3-5 Hz and then 3-10 Hz. The synthetic seismic data were modelled by solving the 2-D elastic-wave equation using a time-domain staggered-grid finite-difference scheme (Levander, 1988) (Text S1). The source wavelets used in synthetic modelling were estimated by stacking the aligned near-offset water arrivals (Text S2 and Figures S3 and S4).

FWI of PmP arrivals is highly nonlinear (Guo *et al.*, 2020) and requires a good initial model and a misfit function that can correctly model the non-linear part of the critically reflected PmP arrivals and also can handle the triplication between Pg, PmP and Pn arrivals around critical angles. We built an initial Vp model (Text S3 and Figure S5) using the tomographic velocity from Canales *et al.* (2003). Comparisons of observed waveforms and the waveform modelled using the initial model show no cycle-skipping in the first stage of FWI, indicating the initial model is close enough to the real velocity of the subsurface. Our FWI workflow was implemented in two stages (Text S4). In the first stage, we applied a trace normalized FWI (Tao *et al.*, 2017) to primarily fit the seismic traveltime (or phase) information, which allows to decouple the complex waveforms associated with the critically reflected PmP arrivals and the triplication and helps to recover the velocity of the MTZ. The result of trace normalized FWI was then used as a starting model for the true amplitude FWI in the second stage. The true amplitude FWI further improves the velocity model as it tries to fit both seismic amplitude and phase information.

The synthetic data after FWI match the observed data very well as compared to those modelled using the tomographic model (Figure 2 and Figure S6). Compared with the starting model (Figure S5A), the velocity model from FWI (Figure 3A) shows fine-scale structures in the crust. We conducted checkerboard tests (Text S5 and Figure S7-S10) to assess the resolution of the FWI result using the same source and receiver geometry as the real data inversion. The checkerboard tests suggest that the FWI can resolve minimum structures of 0.3×8 km size (vertical × horizontal) with 5% velocity anomaly between 10 and 80 km horizontal distance. We also performed synthetic tests (Text S6) to assess the resolvability of the FWI method for a thick or thin MTZ. These synthetic tests indicate that the FWI can recover a MTZ as thin as 0.5 km or as thick as 3.5 km between 10 and 80 km horizontal distance (Figure S11-S17). Therefore, we only interpret the velocity structures between 10 and 80 km horizontal distance.

3. Results

Crustal structure

The upper crust is characterized by low Vp but high vertical velocity gradients (Figures 3A,B,D and E), where the Vp increases rapidly from 3.0±0.1 km/s at the basement to 6.5 km/s at 1.8±0.2 km depth. However, the inverted velocity model reveals a heterogeneous lower crust, where alternate high-and-low-velocity layers are observed (Figures 3A,D and E). We used the contour of vertical velocity gradient of 0 s^{-1} to represent the boundaries between the high- and low-velocity layers (Figure 3B). The thickness of these layers varies from 300-400 m to ~1 km. The maximum velocity reduction within the low-velocity layers is ~500 m/s.

At the base of the model at 8.0-9.5 km depth, a positive high velocity gradient zone is observed (Figure 3B), separating the typical lower crustal velocity above with the mantle velocity below. We picked the depth of the top of this zone, marked by a vertical velocity gradient of 0 s^{-1}, and smoothed it over a horizontal distance of 8 km, which is interpreted as the base of the crust (red dashed curves in Figures 3A,B). This base of the crust shallows from a depth of ~9.5 km between 10 and 20 km distance to ~8.0 km between 45 and 55 km distance, and it lies between 8.2 and 8.5 km depth further north (Figure 3B). The mean velocity at the base of the crust is ~7.0±0.2 km/s, consistent with the global average velocity (7.1±0.1 km/s) at the base of crust formed at fast-spreading ridges (Christeson *et al.*, 2019).

The interpreted crustal base derived from the FWI is shallower than the tomographic Moho from Canales *et al.* (2003) along the entire profile (Figure 3A). The crustal thickness varies between 5.1 and 6.5 km (red curve in Figure 3C) with an average thickness of ~5.6 km, thinner than the average crustal thickness (~6.8 km) obtained from the traveltime tomography (Canales *et al.*, 2003), but close to that (~5.8 km) estimated from the MCS studies in the neighbouring region (Aghaei *et al.*, 2014). The crust is thicker south of the 30-40 km horizontal distance at ~9°36'-9°41'N than to the north, and the thickest crust is observed between 10 and 20 km horizontal distance at ~9°25'-9°30'N (red curve in Figure 3C), which is consistent with the tomography study (Canales *et al.*, 2003) (Figure S3B) and seismic reflection study (Aghaei *et al.*, 2014; Barth and Mutter, 1996). The thinnest crust is observed at 40-60 km horizontal distance at 9°41'-9°51'N, and the crust gradually thickens by ~500 m further north (red curve in Figure 3C).

Moho transition zone (MTZ)

FWI does not provide a sharp boundary for the Moho, but an increase in velocity over a certain depth range, which we define as the MTZ. The base of the crust with zero velocity gradient marks the top of the MTZ. We used two approaches to define the bottom of the MTZ: (I) 7.85 km/s velocity contour, the global average velocity at the top of the mantle (< 7.5 Myr) for crust formed at fast-spreading ridges (Christeson *et al.*, 2019) and (II) the base of the high velocity gradient zone. If we pick the depth of the 7.85 km/s velocity contour (purple dashed curves in Figures 3A,B) the thickness of the MTZ would be between 1.1 and 2.4 km (blue dashed curve in Figure 3C). If we take the base of the large positive velocity gradient zone as the bottom of the MTZ (purple solid curves in Figures 3A,B), the thickness of the MTZ would be between 1.6 and 3.0 km (blue solid curve in Figure 3C) where the average mantle velocity is ~7.97±0.13 km/s. In both cases, the MTZ is relatively thin south of the 30 km horizontal distance at 9°36'N (blue curves in Figure 3C). The thickness of the MTZ shows a negative correlation with the crustal thickness along the profile, i.e., where the MTZ is thick the crust is thin, and vice versa (Figure 3C).

4. Discussion and conclusion

Our results show (I) the presence of layered structures in the lower crust, (II) the crust is thin in the north and thick in the south whereas the MTZ is thick in the north and thin in the south and (III) there is an inverse correlation between the crustal thickness and the MTZ thickness.

Seismic reflection studies of the 9°N EPR have shown the presence of axial melt lens (AML) at 1.4-1.9 km depth in the mid-crust (Detrick *et al.*, 1987; Kent *et al.*, 1993) whereas tomographic studies indicate the presence of low velocity zone down to 6-7 km depth below the seafloor (Dunn, 2022; Dunn *et al.*, 2000), indicating the existence of partial melt. Furthermore, Marjanović *et al.* (2014) and Arnulf *et al.* (2014) show the presence of secondary melt sills within 1.65 km depth below the AML. Studies of the Oman ophiolite suggest that the melt can intrude and crystalize at different depths in the lower crust (Boudier *et al.*, 1996; Kelemen *et al.*, 1997). The observed alternate high-and-low-velocity layering in the lower crust could be due to melt of different compositions injected and crystallised at different depths within the lower crust (Figure 4). The gabbroic rocks drilled from the Hess Deep in the equatorial Pacific are mainly composed of olivine, clinopyroxene and plagioclase (Carlson and Jay Miller, 2004; Lissenberg *et al.*, 2013). A small increase (by 5%) of the olivine content can lead up to 600 m/s increase in Vp of the gabbroic rocks (Carlson and Jay Miller, 2004; Guo *et al.*, 2022). Therefore, the low-velocity layers within the lower crust could be formed by melt with relatively low olivine concentration while the high-velocity layers could represent olivine-rich gabbroic sills. This interpretation supports the 'sheeted sill' model (Boudier *et al.*, 1996; Kelemen *et al.*, 1997) where in-situ melt intrusion and crystallization form the lower crust. Moreover, the off-axis melt sills (Aghaei *et al.*, 2017; Canales *et al.*, 2012; Han *et al.*, 2014) are observed up to a distance of ~12 km from the ridge crest and could form gabbroic sills with different compositions from those formed at the ridge axis, contributing to the formation of a heterogeneous lower crust.

An early study using one-dimensional velocity analysis found that the MTZ at ~9º35'N EPR is ~1.7 km at 10 km off-axis distance (Vera *et al.*, 1990). Another MCS study from the intermediate-spreading Juan de Fuca Ridge observed that the MTZ could be up to 2.0 km thick (Nedimović *et al.*, 2005). These estimates fall in the ranges of MTZ thickness obtained using FWI, but our results provide a 2-D view continuous over 70 km distance along the profile and its relationship to crustal structure.

There are two possibilities for the above observations. The along-strike variations in the MTZ thickness could be due to the different thermal structures among third-order discontinuities. Thermal structure plays an important role in controlling the vertical depth of melt introduction and crystallization at fast-spreading ridges (Maclennan *et al.*, 2004). For a relatively hot ridge segment, melt will pool and crystalize at shallower depth in the lower crust with little melt accumulate within the MTZ. In contrast, for a relatively cold ridge segment, some melt could accumulate at deeper depths in the lower crust or at Moho depth, forming a thick MTZ. Presence of melt around Moho depth beneath the 9-10^{o}N EPR has been observed in the seafloor compliance (Crawford *et al.*, 1991). The along-strike variations in the MTZ thickness could also reflect changes in the efficiency of melt migration through the MTZ beneath the spreading centre. A thin MTZ would indicate a rapid percolation of melt from the upwelling mantle to the accreting crust. The formation of a thick MTZ could be due to less efficient melt extraction from mantle to crust leading to the accumulation and crystallization of a large amount of melt within the transition zone (Figure 4). Melt crystallization might occur in the thin MTZ as well.

These interpretations are supported by the negative correlation between the thicknesses of the crust and MTZ. A relatively thick MTZ underlying a relatively thin crust suggests that a significant part of melt was crystallized in the MTZ. However, the total cumulative thickness of the crust and MTZ does not vary much along the profile, albeit the total melt supply from the mantle to crust might be uniform along the entire ridge segment.

Based on the study of Oman ophiolite, Nicolas *et al.* (1996) found that the thin lower crust is generally associated with a thick MTZ while the thick lower crust is associated with a thin MTZ, indicating that there is an anti-correlation between the ophiolite's crustal and MTZ thicknesses, assuming the combined thickness of the extrusive basalt and sheeted dike is constant. The extensive presence of thick gabbro sills observed in the relatively thick MTZ in the Oman ophiolite demonstrate that a large amount of magma has ponded within the MTZ (Boudier and Nicolas, 1995), supporting our interpretation.

Along our profile, the change from a relatively thin to thick MTZ occurs over a short distance of ~10 km (Figure 3C), and a similar pattern has been observed in the Oman ophiolite where the transition from a thin to thick MTZ occurs over <5 km distance (Jousselin and Nicolas, 2000). The seismic reflection study at 9ºN EPR (Aghaei *et al.*, 2014) also found that the character of the Moho reflection varies over 3-4 km spatial distance. Given different lateral resolutions of these methods, these observations indicate that the thermal structure and/or melt migration efficiency through MTZ can vary quickly along the ridge axis at fast-spreading ridge. Laterally abrupt changes in the thermal structure and melt migration efficiency will influence ridge segmentation, possibly governing the distributions of third-order ridge discontinuities (Aghaei *et al.*, 2014).

The average crustal thickness estimated from MCS data is ~5.8 km in the 9ºN EPR region (Aghaei *et al.*, 2014). However, seismic refraction study in the neighbouring region suggests ~1 km thicker crust (Canales *et al.*, 2003). This indicates a discrepancy in the oceanic crustal thickness obtained using seismic refraction and reflection methods, though these study areas are not exactly the same. The Moho depths estimated from reflection and refraction studies appear to have good consistency at some regions close to subduction trenches in the Pacific Ocean (Ivandic *et al.*, 2008; Kodaira *et al.*, 2014). However, in these studies, the Moho depths estimated from OBS data show large uncertainties of the order of ~1 km. In contrast, FWI of wide-angle seismic data can provide precise velocity of the crust and upper mantle and constrain the thickness of the MTZ, reconciling the discrepancy between the seismic reflection and the refraction methods. Our results demonstrate that the FWI method is a powerful tool for understanding the structures of crust and MTZ and crustal accretion processes at MORs.

Figures

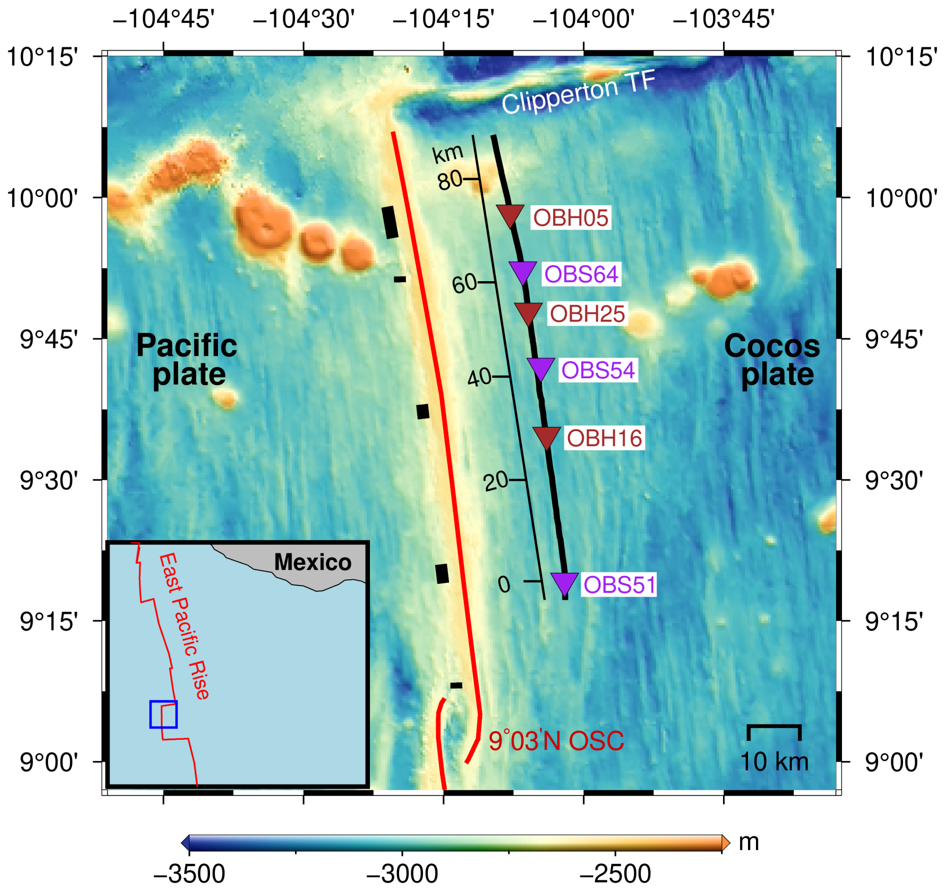

Figure 1. Bathymetry map of the study area. Red curves show the East Pacific Rise between the Clipperton transform fault (TF) and the 9°03’N overlapping spreading centre (OSC). The black rectangles show the locations of third-order discontinuities at 9°12’N, 9°20’N, 9°37’N, 9°51.5’N and 9°58’N from south to north, respectively (Aghaei *et al.*, 2014; White *et al.*, 2006). The black line indicates the seismic profile. Brown and purple triangles represent the locations of ocean bottom hydrophones (OBHs) and ocean bottom seismometers (OBSs), respectively. The blue box in the inset shows the location of the study area. The black scale shows the distance along the profile.

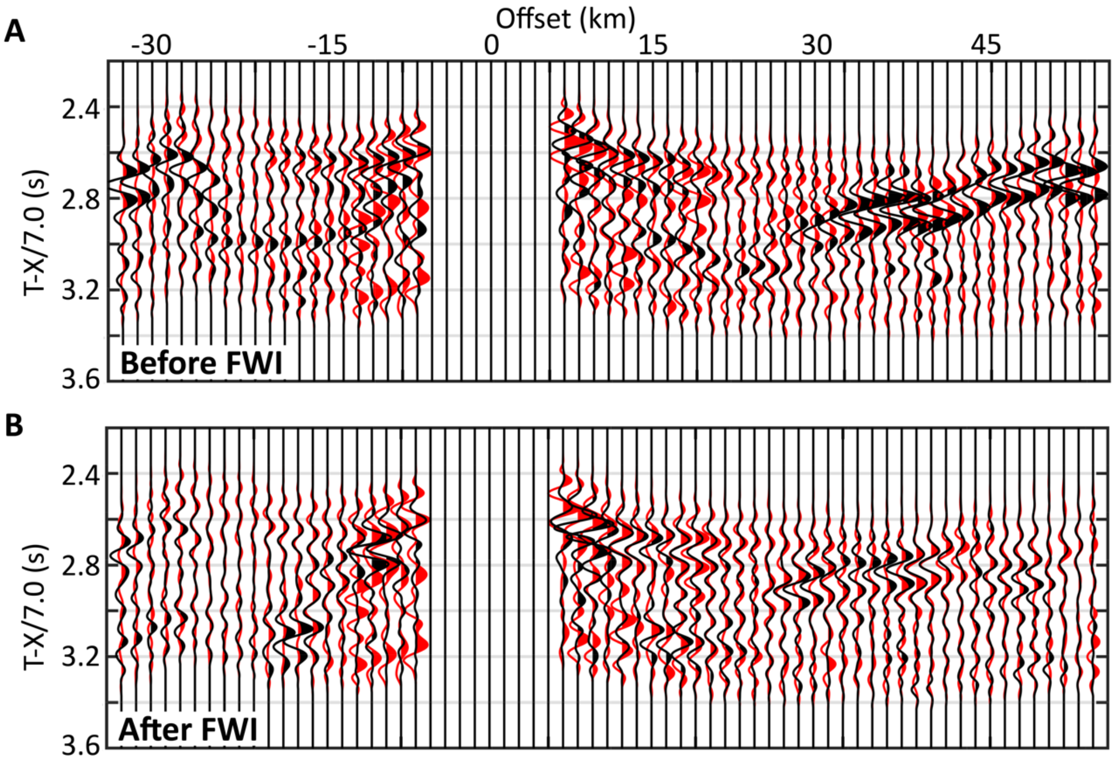

Figure 2. Comparisons of modelled and observed seismic data for OBH25. (A) Before FWI and (B) after FWI. The observed data is filtered to 3-10 Hz and the modelled data are calculated using the 3-10 Hz source wavelet. The modelled and observed seismic data are plotted in black and red, respectively. Traveltime (T) of the seismic data is reduced using a reduction velocity of 7.0 km/s. For better visibility, a scalar weighting factor ($1 + 0.1 \times X$) was applied for each trace to enhance the amplitude at large offsets, where X is the offset.

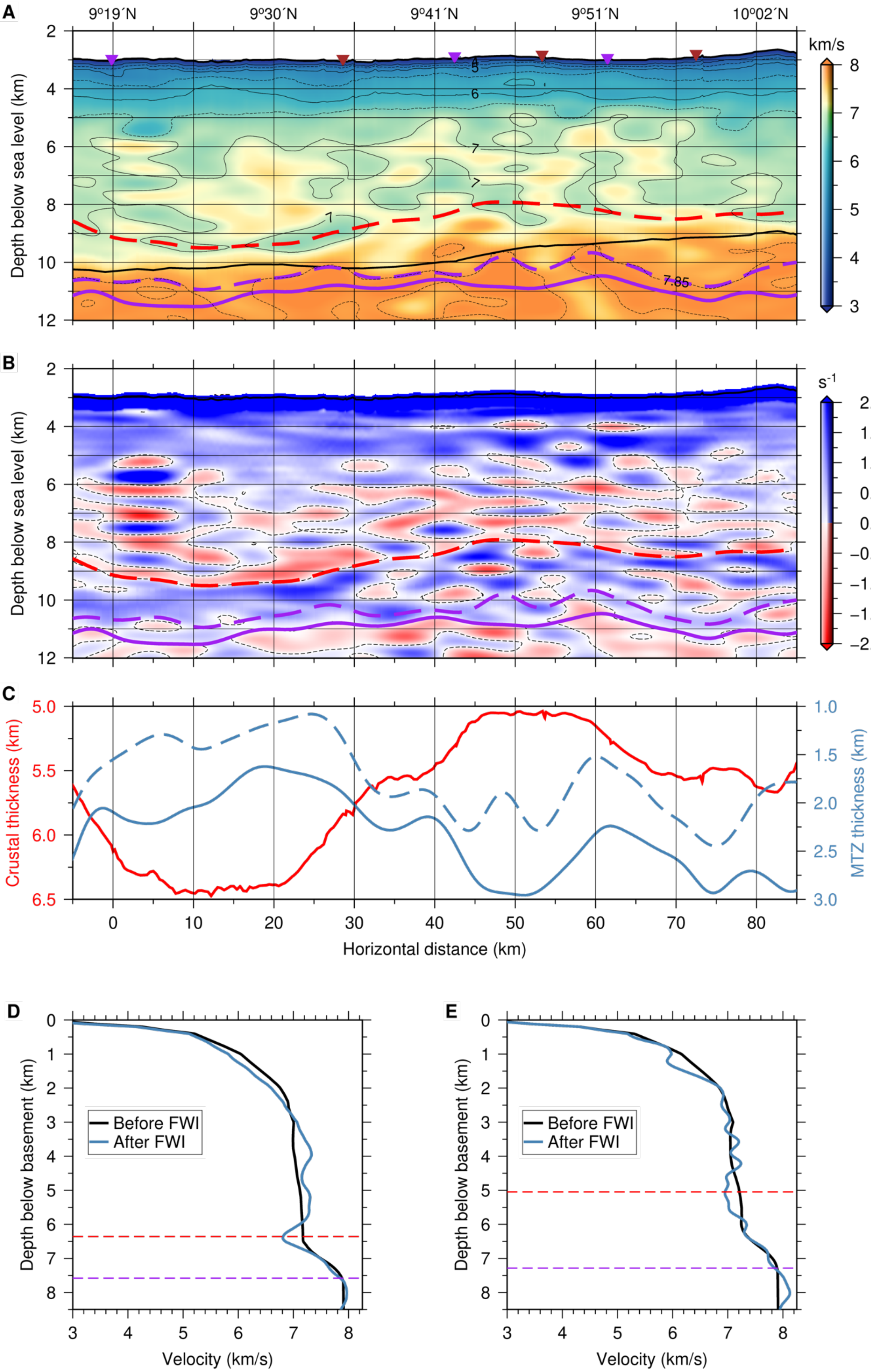

A
9º19´N
9º30´N
9º41´N
9º51´N
10º02´N
km/s
Depth below sea level (km)
7.85
B
s-1
Depth below sea level (km)
C
Crustal thickness (km)
MTZ thickness (km)
Horizontal distance (km)
D
Depth below basement (km)
Before FWI
After FWI
Velocity (km/s)
E
Depth below basement (km)
Before FWI
After FWI
Velocity (km/s)

Figure 3. Results of FWI. (A) Crustal and upper mantle P-wave velocity model from FWI. The thick black curve is the tomographic Moho from Canales *et al.* (2003). The red dashed curve is the interpreted crustal base corresponding to the top of the large positive velocity gradient zone beneath the crust. The dashed purple curve is the bottom of the MTZ interpreted using a smooth version of the 7.85 km/s velocity contour (Christeson *et al.*, 2019). The solid purple curve is the bottom of the MTZ interpreted using the base of the large positive velocity gradient zone. The 4.5, 5.5, 6.5 and 7.85 km/s velocity contours are shown as black dashed curves from top to bottom. The brown and purple triangles show the locations of OBHs and OBSs, respectively. (B) Vertical velocity gradient. The black dashed curves are the 0 s^{-1} velocity gradient contour. The red and the purple curves are the same as in A. (C) The crustal (in red) and the MTZ thickness (in blue) variations along the profile. The blue dashed and solid curves are the MTZ thickness calculated using a smooth version of the 7.85 km/s velocity contour (purple dashed curves in A,B) and using the base of the large positive velocity gradient zone (purple solid curves in A,B) as the bottom of the MTZ, respectively. (D) Comparison of the starting (in black) and final (in blue) inverted velocity profiles averaged between 16 and 24 km horizontal distance where the crust is thick and the MTZ is thin. (E) Comparison of the starting (in black) and final (in blue) inverted velocity profiles averaged between 46 and 54 km horizontal distance where the crust is thin and the MTZ is thick. The red and purple dashed lines in d and e represent the top of the MTZ and the MTZ bottom defined by 7.85 km/s velocity contour.

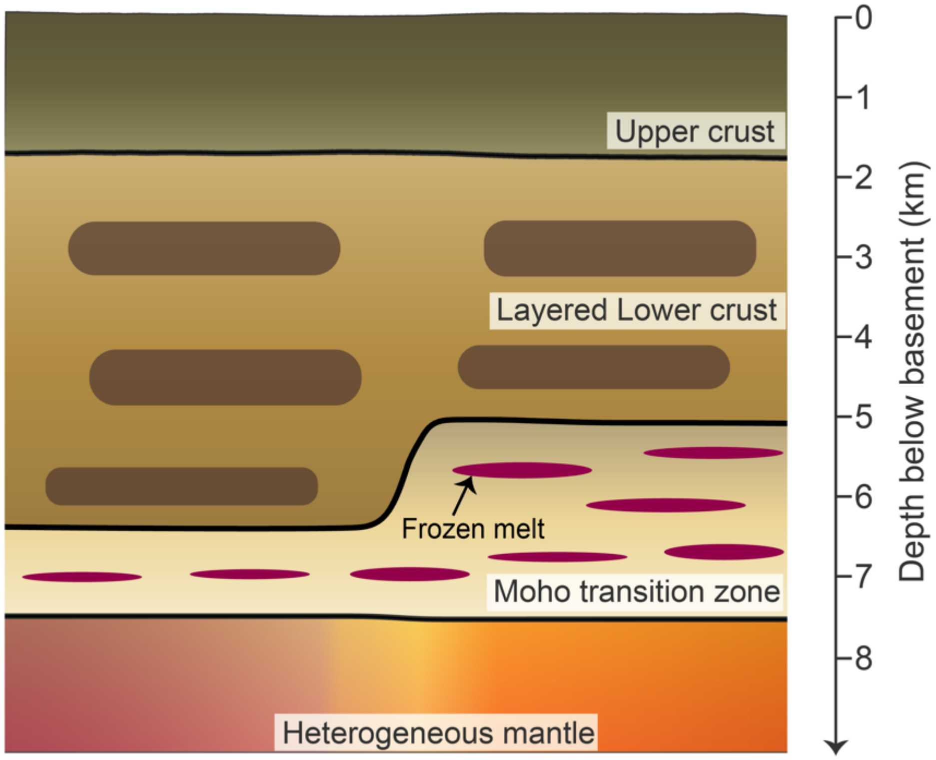

Figure 4. Schematic diagram showing structures of the oceanic crust and Moho transition zone (MTZ). The oceanic crust is separated into an upper crust (~1.8 km thick) and a layered lower crust. The dark brown blocks in the lower crust refer to the low-velocity layers from FWI. The layered lower crust indicates the oceanic lower crust is formed by in-situ melt injection and crystallization at different depths. The thickness of the MTZ varies along strike between 1.1 and 2.4 km, inversely correlated with the crustal thickness. The red horizontal elongated ellipsoids represent the frozen gabbro sills, which is accumulated and crystalized during its migration from the upwelling mantle to the crust.

REFERENCES

Aghaei, O., M. R. Nedimović, H. Carton, S. M. Carbotte, J. P. Canales, and J. C. Mutter (2014), Crustal thickness and Moho character of the fast-spreading East Pacific Rise from 9° 42′N to 9°57′N from poststack-migrated 3-D MCS data, *Geochem. Geophys. Geosyst.*, *15*(3), 634-657, doi:https://doi.org/10.1002/2013GC005069.

Aghaei, O., M. R. Nedimović, M. Marjanović, S. M. Carbotte, J. Pablo Canales, H. Carton, and N. Nikić (2017), Constraints on melt content of off-axis magma lenses at the East Pacific Rise from analysis of 3-D seismic amplitude variation with angle of incidence, *J. Geophys. Res.*, *122*(6), 4123-4142, doi:https://doi.org/10.1002/2016JB013785.

Arnulf, A. F., S. C. Singh, and J. W. Pye (2014), Seismic evidence of a complex multi-lens melt reservoir beneath the 9° N Overlapping Spreading Center at the East Pacific Rise, *Geophys. Res. Lett.*, *41*(17), 6109-6115, doi:https://doi.org/10.1002/2014GL060859.

Barth, G. A., and J. C. Mutter (1996), Variability in oceanic crustal thickness and structure: Multichannel seismic reflection results from the northern East Pacific Rise, *J. Geophys. Res.*, *101*(B8), 17951-17975, doi:https://doi.org/10.1029/96JB00814.

Benn, K., A. Nicolas, and I. Reuber (1988), Mantle—crust transition zone and origin of wehrlitic magmas: Evidence from the Oman ophiolite, *Tectonophysics*, *151*(1), 75-85, doi:https://doi.org/10.1016/0040-1951(88)90241-7.

Boudier, F., and A. Nicolas (1995), Nature of the Moho Transition Zone in the Oman Ophiolite, *J. Petrol.*, *36*(3), 777-796, doi:10.1093/petrology/36.3.777.

Boudier, F., A. Nicolas, and B. Ildefonse (1996), Magma chambers in the Oman ophiolite: fed from the top and the bottom, *Earth Planet. Sci. Lett.*, *144*(1), 239-250, doi:https://doi.org/10.1016/0012-821X(96)00167-7.

Brocher, T. M., J. A. Karson, and J. A. Collins (1985), Seismic stratigraphy of the oceanic Moho based on ophiolite models, *Geology*, *13*(1), 62-65, doi:10.1130/0091-7613(1985)13<62:Ssotom>2.0.Co;2.

Canales, J. P., H. Carton, S. M. Carbotte, J. C. Mutter, M. R. Nedimović, M. Xu, O. Aghaei, M. Marjanović, and K. Newman (2012), Network of off-axis melt bodies at the East Pacific Rise, *Nature Geosci.*, *5*(4), 279-283, doi:10.1038/ngeo1377.

Canales, P. J., R. S. Detrick, D. R. Toomey, and W. S. D. Wilcock (2003), Segment-scale variations in the crustal structure of 150–300 kyr old fast spreading oceanic crust (East Pacific Rise, 8°15′N–10°5′N) from wide-angle seismic refraction profiles, *Geophys. J. Int.*, *152*(3), 766-794, doi:10.1046/j.1365-246X.2003.01885.x.

Cann, J. R. (1970), New Model for the Structure of the Ocean Crust, *Nature*, *226*(5249), 928-930, doi:10.1038/226928a0.

Carlson, R. L., and D. Jay Miller (2004), Influence of pressure and mineralogy on seismic velocities in oceanic gabbros: Implications for the composition and state of the lower oceanic crust, *J. Geophys. Res.*, *109*(B9), B09205, doi:https://doi.org/10.1029/2003JB002699.

Christeson, G. L., J. A. Goff, and R. S. Reece (2019), Synthesis of Oceanic Crustal Structure From Two-Dimensional Seismic Profiles, *Rev. Geophys.*, *57*(2), 504-529, doi:https://doi.org/10.1029/2019RG000641.

Collins, J. A., T. M. Brocher, and J. A. Karson (1986), Two-dimensional seismic reflection modeling of the inferred fossil oceanic crust/mantle transition in the Bay of Islands Ophiolite, *J. Geophys. Res.*, *91*(B12), 12520-12538, doi:https://doi.org/10.1029/JB091iB12p12520.

Crawford, W. C., S. C. Webb, and J. A. Hildebrand (1991), Seafloor compliance observed by long-period pressure and displacement measurements, *J. Geophys. Res.*, *96*(B10), 16151-16160, doi:https://doi.org/10.1029/91JB01577.

Detrick, R. S., P. Buhl, E. Vera, J. Mutter, J. Orcutt, J. Madsen, and T. Brocher (1987), Multi-channel seismic imaging of a crustal magma chamber along the East Pacific Rise, *Nature*, *326*(6108), 35-41, doi:10.1038/326035a0.

Dunn, R. A. (2022), A Dual-Level Magmatic System Beneath the East Pacific Rise, 9°N, *Geophys. Res. Lett.*, *49*(18), e2022GL097732, doi:https://doi.org/10.1029/2022GL097732.

Dunn, R. A., D. R. Toomey, and S. C. Solomon (2000), Three-dimensional seismic structure and physical properties of the crust and shallow mantle beneath the East Pacific Rise at 9°30'N, *J. Geophys. Res.*, *105*(B10), 23537-23555, doi:https://doi.org/10.1029/2000JB900210.

Guo, P., S. C. Singh, V. Vaddineni, I. Grevemeyer, and E. Saygin (2022), Lower oceanic crust formed by in situ melt crystallization revealed by seismic layering, *Nature Geosci.*, *15*, 591–596, doi:https://doi.org/10.1038/s41561-022-00963-w.

Guo, P., S. C. Singh, V. A. Vaddineni, G. Visser, I. Grevemeyer, and E. Saygin (2020), Nonlinear full waveform inversion of wide-aperture OBS data for Moho structure using a trans-dimensional Bayesian method, *Geophys. J. Int.*, *224*(2), 1056-1078, doi:10.1093/gji/ggaa505.

Han, S., S. M. Carbotte, H. Carton, J. C. Mutter, O. Aghaei, M. R. Nedimović, and J. P. Canales (2014), Architecture of on- and off-axis magma bodies at EPR 9°37–40′N and implications for oceanic crustal accretion, *Earth Planet. Sci. Lett.*, *390*, 31-44, doi:https://doi.org/10.1016/j.epsl.2013.12.040.

Ivandic, M., I. Grevemeyer, A. Berhorst, E. R. Flueh, and K. McIntosh (2008), Impact of bending related faulting on the seismic properties of the incoming oceanic plate offshore of Nicaragua, *J. Geophys. Res.*, *113*(B5), doi:https://doi.org/10.1029/2007JB005291.

Jian, H., M. R. Nedimović, J. P. Canales, and K. W. H. Lau (2021), New Insights Into the Rift to Drift Transition Across the Northeastern Nova Scotian Margin From Wide-Angle Seismic Waveform Inversion and Reflection Imaging, *J. Geophys. Res.*, *126*(12), e2021JB022201, doi:https://doi.org/10.1029/2021JB022201.

Jousselin, D., and A. Nicolas (2000), The Moho transition zone in the Oman ophiolite-relation with wehrlites in the crust and dunites in the mantle, *Mar. Geophys. Res.*, *21*(3), 229-241, doi:10.1023/A:1026733019682.

Karson, J. A., J. A. Collins, and J. F. Casey (1984), Geologic and seismic velocity structure of the crust/mantle transition in the Bay of Islands Ophiolite Complex, *J. Geophys. Res.*, *89*(B7), 6126-6138, doi:https://doi.org/10.1029/JB089iB07p06126.

Kelemen, P. B., K. Koga, and N. Shimizu (1997), Geochemistry of gabbro sills in the crust-mantle transition zone of the Oman ophiolite: implications for the origin of the oceanic lower crust, *Earth Planet. Sci. Lett.*, *146*(3), 475-488, doi:https://doi.org/10.1016/S0012-821X(96)00235-X.

Kent, G. M., A. J. Harding, and J. A. Orcutt (1993), Distribution of magma beneath the East Pacific Rise between the Clipperton Transform and the 9°17′N Deval from forward modeling of common depth point data, *J. Geophys. Res.*, *98*(B8), 13945-13969, doi:https://doi.org/10.1029/93JB00705.

Kent, G. M., A. J. Harding, J. A. Orcutt, R. S. Detrick, J. C. Mutter, and P. Buhl (1994), Uniform accretion of oceanic crust south of the Garrett transform at 14°15′S on the East Pacific Rise, *J. Geophys. Res.*, *99*(B5), 9097-9116, doi:https://doi.org/10.1029/93JB02872.

Kodaira, S., G. Fujie, M. Yamashita, T. Sato, T. Takahashi, and N. Takahashi (2014), Seismological evidence of mantle flow driving plate motions at a palaeo-spreading centre, *Nature Geosci.*, *7*(5), 371-375, doi:10.1038/ngeo2121.

Levander, A. R. (1988), Fourth-order finite-difference P-SV seismograms, *Geophysics*, *53*(11), 1425-1436, doi:10.1190/1.1442422.

Lissenberg, C. J., C. J. MacLeod, K. A. Howard, and M. Godard (2013), Pervasive reactive melt migration through fast-spreading lower oceanic crust (Hess Deep, equatorial Pacific Ocean), *Earth Planet. Sci. Lett.*, *361*, 436-447, doi:https://doi.org/10.1016/j.epsl.2012.11.012.

Maclennan, J., T. Hulme, and S. C. Singh (2004), Thermal models of oceanic crustal accretion: Linking geophysical, geological and petrological observations, *Geochem. Geophys. Geosyst.*, *5*(2), doi:https://doi.org/10.1029/2003GC000605.

Marjanović, M., S. M. Carbotte, H. Carton, M. R. Nedimović, J. C. Mutter, and J. P. Canales (2014), A multi-sill magma plumbing system beneath the axis of the East Pacific Rise, *Nature Geosci.*, *7*(11), 825-829, doi:10.1038/ngeo2272.

Mutter, J. C., G. A. Barth, P. Buhl, R. S. Detrick, J. Orcutt, and A. Harding (1988), Magma distribution across ridge-axis discontinuities on the East Pacific Rise from multichannel seismic images, *Nature*, *336*(6195), 156-158, doi:10.1038/336156a0.

Nedimović, M. R., S. M. Carbotte, A. J. Harding, R. S. Detrick, J. P. Canales, J. B. Diebold, G. M. Kent, M. Tischer, and J. M. Babcock (2005), Frozen magma lenses below the oceanic crust, *Nature*, *436*(7054), 1149-1152, doi:10.1038/nature03944.

Nicolas, A., F. Boudier, and B. Ildefonse (1996), Variable crustal thickness in the Oman ophiolite: Implication for oceanic crust, *J. Geophys. Res.*, *101*(B8), 17941-17950, doi:https://doi.org/10.1029/96JB00195.

Pica, A., J. P. Diet, and A. Tarantola (1990), Nonlinear inversion of seismic reflection data in a laterally invariant medium, *Geophysics*, *55*(3), 284-292, doi:10.1190/1.1442836.

Shipp, R. M., and S. C. Singh (2002), Two-dimensional full wavefield inversion of wide-aperture marine seismic streamer data, *Geophys. J. Int.*, *151*(2), 325-344, doi:10.1046/j.1365-246X.2002.01645.x.

Tao, K., S. P. Grand, and F. Niu (2017), Full-waveform inversion of triplicated data using a normalized-correlation-coefficient-based misfit function, *Geophys. J. Int.*, *210*(3), 1517-1524, doi:10.1093/gji/ggx249.

Toomey, D. R., R. S. Detrick, and W. S. D. Wilcock (1997), Mapping melt and matrix flow in the uppermost mantle: undershooting the East Pacific Rise between the Siqueiros and Clipperton, R/V Maurice Ewing Leg 97–08, *Cruise Report, p. 163, Woods Hole Oceanogr. Inst., Woods Hole, MA.*

Vaddineni, V. A., S. C. Singh, I. Grevemeyer, P. Audhkhasi, and C. Papenberg (2021), Evolution of the Crustal and Upper Mantle Seismic Structure From 0–27 Ma in the Equatorial Atlantic Ocean at 2° 43′S, *J. Geophys. Res.*, *126*(6), e2020JB021390, doi:https://doi.org/10.1029/2020JB021390.

Vera, E. E., J. C. Mutter, P. Buhl, J. A. Orcutt, A. J. Harding, M. E. Kappus, R. S. Detrick, and T. M. Brocher (1990), The structure of 0- to 0.2-m.y.-old oceanic crust at 9°N on the East Pacific Rise from expanded spread profiles, *J. Geophys. Res.*, *95*(B10), 15529-15556, doi:doi:10.1029/JB095iB10p15529.

Virieux, J., and S. Operto (2009), An overview of full waveform inversion in exploration geophysics, *Geophysics*, *74*(6), WCC1–WCC26, doi:https://doi.org/10.1190/1.3238367.

Wang, Z., and S. C. Singh (2022), Seismic evidence for uniform crustal accretion along slow-spreading ridges in the equatorial Atlantic Ocean, *Nat. Commun.*, *13*(1), 7809, doi:10.1038/s41467-022-35459-z.

Wang, Z., S. C. Singh, and J. P. Canales (2024), Wide-angle seismic refraction data from the northern portion of the outer eastern profile, 9°N East Pacific Rise, *IPGP Research Collection*, url:https://dataverse.ipgp.fr/privateurl.xhtml?token=6eca5518-ffd6-4737-a016-32f5d28f5fea.

White, R. S., D. McKenzie, and R. K. O'Nions (1992), Oceanic crustal thickness from seismic measurements and rare earth element inversions, *J. Geophys. Res.*, *97*(B13), 19683-19715, doi:https://doi.org/10.1029/92JB01749.

White, S. M., R. M. Haymon, and S. Carbotte (2006), A new view of ridge segmentation and near-axis volcanism at the East Pacific Rise, 8°–12°N, from EM300 multibeam bathymetry, *Geochem. Geophys. Geosyst.*, *7*(12), doi:https://doi.org/10.1029/2006GC001407.

Acknowledgements

We thank the captain, crew and scientific team of the R/V Maurice Ewing Leg 97-08 for the data collection. Acquisition of the data used in this study was supported by NSF Award OCE-9634132. Z. Wang's contributions to this work were supported by the postdoctoral fellowship from the GPX project of Institut de Physique du Globe de Paris and partially by the Newton International Fellowships from the Royal Society. J.P. Canales' contributions to this study were supported by NSF Award OCE-0118383 and by the Independent Research & Development Program at WHOI. Results presented in this paper were performed either on the S-CAPAD platform of Institut de Physique du Globe de Paris or on the IRIDIS High Performance Computing Facility of the University of Southampton, and we acknowledge the associated support services in the completion of this work.

Author Contributions

Z.W. processed the data and wrote the paper. S.C.S. developed the project, supervised the data processing and wrote the paper. J.P.C. provided the tomographic velocity model. All authors discussed the results, participated in interpretation, and contributed to paper writing.

Competing Interests

The authors declare that they have no competing interests.

Open Research

The seismic data used in this study are available at the Institut de Physique du Globe de Paris (IPGP) Research Collection (Wang *et al.*, 2024).

Link between crustal thickness and Moho transition zone at 9ºN East Pacific Rise

Zhikai Wang[1,2], Satish C. Singh[1], and J. Pablo Canales[3]

[1] Institut de Physique du Globe de Paris, Université Paris Cité, 1 Rue Jussieu, 75005 Paris, France.

[2] Presently at School of Ocean and Earth Science, University of Southampton, European Way, SO14 3ZH Southampton, UK.

[3] Department of Geology and Geophysics, Woods Hole Oceanographic Institution, Woods Hole MA 02543, USA.

Abstract

Oceanic crust at fast-spreading ridges is formed by melt percolating through the Mohorovičić Transition Zone (MTZ), the boundary between crust and mantle. However, the relationship between the crustal structures and MTZ remains elusive. Applying full waveform inversion to wide-angle seismic data acquired near the 9ºN East Pacific Rise, we show that the variations in crustal MTZ thicknesses are inversely correlated along the segment, although their total cumulative thickness shows little variations. These variations could be attributed to different melt migration efficiency through MTZ or variation in mantle thermal structures. Thin MTZ could be due to rapid percolation of melt from mantle to crust whereas the thick MTZ results from the crystallization of melt within the transition zone. On the other hand, for relatively hot segments, melt will accumulate at shallower depth within the lower crust. In contrast, melt could freeze at Moho depth for relatively cold segments thickening the MTZ.

Plain Language Summary

At the spreading centres where two plates move apart, the basaltic melt produced by decompression melting of the upwelling mantle forms new oceanic crust. The oceanic crust is separated from the underlying mantle by the Mohorovičić Transition Zone (MTZ). However, the relationship between the crustal structures and MTZ is poorly known. We applied seismic full waveform inversion, a state-of-the-art seismic imaging method, to the wide-angle seismic data collected from a young oceanic crust near the 9°N East Pacific Rise. We found that the crustal thickness varies from 5.1 to 6.5 km along a 70 km-long crustal segment. Interestingly, the MTZ thickness varies between 1.1 to 2.4 km along the segment and is inversely correlated with crustal thickness. The total cumulative thickness of crust and MTZ keeps almost constant along the profile. These variations could be explained either by different melt migration efficiency through MTZ or by changes in mantle thermal structures along the ridge segment.

Key points:

- We apply elastic-wave full waveform inversion to wide-angle seismic data acquired near the 9°N East Pacific Rise
- The high-resolution crustal velocity model shows that the crustal thickness varies between 5.1 and 6.5 km along a 70 km-long crustal segment
- The thickness of Moho transition zone is inversely correlated with crustal thickness along the segment

1. Introduction

Oceanic crust is formed at mid-ocean ridges (MORs) from basaltic melt derived from decompression of upwelling mantle as two lithospheric plates move apart (Cann, 1970). In a fast and intermediate-spreading environment, the melt rises towards the surface and accumulates within an axial magma chamber (AMC) at mid-crustal depths (Detrick *et al.*, 1987; Mutter *et al.*, 1988). A portion of the accumulated melt erupts to form lava flows on the seafloor and dike underneath, making up the upper crust. The remainder of the melt crystallises within the AMC, forming the gabbroic lower crust. The crust is separated from the underlying mantle by the Moho Transition Zone (MTZ). Determining the relationship between the oceanic crustal structure and the MTZ is critical for understanding the crustal accretion at MORs.

Traveltime tomography of wide-angle seismic refraction data has revealed that the magmatic crust consists of two layers: an upper crust characterised by low P-wave velocities (Vp: 3.0-6.5 km/s) but high velocity gradients and a lower crust exhibiting high Vp (6.5-7.1 km/s) and significantly reduced velocity gradient (Christeson *et al.*, 2019; White *et al.*, 1992). The mantle underneath has a Vp >7.7 km/s and consists primarily of peridotite (Christeson *et al.*, 2019; Wang and Singh, 2022). However, traveltime tomography constrains the lower crustal velocity using wide-angle reflections (PmP) from the Moho, resulting in a trade-off between the lower crustal velocity and the Moho depth (Vaddineni *et al.*, 2021). Furthermore, the Moho is commonly assumed to be a sharp interface in traveltime tomography (Canales *et al.*, 2003; Vaddineni *et al.*, 2021; Wang and Singh, 2022), which has precluded determining the relationship between the crustal structure and the MTZ.

Multi-channel seismic (MCS) data provide reflection images of the oceanic Moho formed at fast- and intermediate-spreading ridges with seismic characters ranging from impulsive, shingled and diffusive (Aghaei *et al.*, 2014; Kent *et al.*, 1994). The impulsive and shingled Moho are characterized by a single-phase reflection while the diffusive Moho shows sub-horizontally multi-phase reflection events (Aghaei *et al.*, 2014; Barth and Mutter, 1996; Kent *et al.*, 1994). Seismic waveform modelling demonstrates that the impulsive and shingled Moho reflections are probably produced by a thin MTZ and the diffusive Moho indicates a relatively thick MTZ (Brocher *et al.*, 1985; Collins *et al.*, 1986). Nedimović *et al.* (2005) suggest that the multi-phase Moho reflection events might be caused by the frozen magma lenses within a thick MTZ. However, MCS data provide the Moho structure in two-way traveltime, which needs to be converted to depth. Due to the lack of accurate velocity model of the subsurface, the uncertainty in the inferred Moho depth can be hundreds metres (Aghaei *et al.*, 2014; Barth and Mutter, 1996), and even >1 km in some cases (Barth and Mutter, 1996). Therefore, our understanding of MTZ from seismic methods remain elusive.

Structural mapping of ophiolites, which are thought to be formed at ancient spreading ridges, indicates that the MTZ is primarily composed of dunites with gabbroic sills and lenses, marking a gradually downward change from layered gabbro in the lower crust to ultramafic mantle consisting dominantly of harzburgites (Benn *et al.*, 1988; Boudier and Nicolas, 1995; Karson *et al.*, 1984). The thickness of the MTZ varies from 5-10 m to 1-3 km (Benn *et al.*, 1988; Karson *et al.*, 1984), where the thickness of gabbroic sills and lenses can reach hundreds of meters in a thick MTZ (Benn *et al.*, 1988; Boudier and Nicolas, 1995; Karson *et al.*, 1984). The strong magmatic flow structures within the MTZ indicate that these gabbroic sills were emplaced at the ridge axis, implying that a large amount of melt was trapped within the MTZ during crustal accretion (Boudier and Nicolas, 1995). However, in the absence of drilling results, we do not have any in situ information about the MTZ.

Here, we present results of the application of two-dimensional (2-D) elastic full waveform inversion (FWI) (Shipp and Singh, 2002) to wide-angle seismic data to constrain the Vp of the crust and MTZ of young oceanic crust near the East Pacific Rise (EPR) at 9°-10°N. FWI can provide high-resolution velocity model of the subsurface at a vertical resolution of half a wavelength (Virieux and Operto, 2009), i.e. hundreds meter (Guo *et al.*, 2022; Jian *et al.*, 2021), important for studying the fine-scale structures of oceanic crust and MTZ.

2. Seismic data and full waveform inversion

The seismic data were acquired from the fast-spreading (11 cm/yr) EPR between 8°15'N and 10°05'N during the 1997 Undershoot Seismic Experiment (Toomey *et al.*, 1997). Although the undershoot experiment was performed covering the whole 9°N EPR segment on both flanks (Toomey *et al.*, 1997), here we use only six ocean bottom instruments deployed at dominantly ~8-14 km intervals along a 92 km-long profile on the eastern flank of the EPR (Figure 1) between the Clipperton transform fault (TF; first-order discontinuity) and the 9°03'N overlapping spreading centre (OSC; second-order discontinuity). The EPR between the 9°03'N OSC and the Clipperton TF is further offset by the third-order discontinuities at 9°12'N, 9°20'N, 9°37'N, 9°51.5'N and 9°58'N, respectively (black rectangles in Figure 1; (Aghaei *et al.*, 2014; White *et al.*, 2006)). The source was an airgun array with a total volume of 8503 in^3, towed at 10 m depth and fired at ~ 460 m interval.

We simultaneously inverted the pressure data recorded by ocean bottom hydrophones (OBHs) and the vertical component data of ocean bottom seismometers (OBSs). We band-pass filtered the data between 3 and 30 Hz and applied a predictive gapped deconvolution with minimum and maximum lags of 0.14 s and 0.35 s to suppress the seismic bubbles (Figure S1). The deconvolved data were transformed from three-dimensional (3-D) to 2-D by multiplying the amplitude of the data by $\sqrt{t}$ (where t is the traveltime) and convolving the seismic data with $1/\sqrt{t}$ (Pica *et al.*, 1990). A 1.0 s-wide time windowing was applied to extract the Pg, PmP and mantle refraction (Pn) arrivals between 6 and 60 km offsets (Figure S2). The top of the time window is 0.1 s prior the picked first arrival traveltime. In this work, we inverted the seismic data of two frequency bands, first 3-5 Hz and then 3-10 Hz. The synthetic seismic data were modelled by solving the 2-D elastic-wave equation using a time-domain staggered-grid finite-difference scheme (Levander, 1988) (Text S1). The source wavelets used in synthetic modelling were estimated by stacking the aligned near-offset water arrivals (Text S2 and Figures S3 and S4).

FWI of PmP arrivals is highly nonlinear (Guo *et al.*, 2020) and requires a good initial model and a misfit function that can correctly model the non-linear part of the critically reflected PmP arrivals and also can handle the triplication between Pg, PmP and Pn arrivals around critical angles. We built an initial Vp model (Text S3 and Figure S5) using the tomographic velocity from Canales *et al.* (2003). Comparisons of observed waveforms and the waveform modelled using the initial model show no cycle-skipping in the first stage of FWI, indicating the initial model is close enough to the real velocity of the subsurface. Our FWI workflow was implemented in two stages (Text S4). In the first stage, we applied a trace normalized FWI (Tao *et al.*, 2017) to primarily fit the seismic traveltime (or phase) information, which allows to decouple the complex waveforms associated with the critically reflected PmP arrivals and the triplication and helps to recover the velocity of the MTZ. The result of trace normalized FWI was then used as a starting model for the true amplitude FWI in the second stage. The true amplitude FWI further improves the velocity model as it tries to fit both seismic amplitude and phase information.

The synthetic data after FWI match the observed data very well as compared to those modelled using the tomographic model (Figure 2 and Figure S6). Compared with the starting model (Figure S5A), the velocity model from FWI (Figure 3A) shows fine-scale structures in the crust. We conducted checkerboard tests (Text S5 and Figure S7-S10) to assess the resolution of the FWI result using the same source and receiver geometry as the real data inversion. The checkerboard tests suggest that the FWI can resolve minimum structures of 0.3×8 km size (vertical × horizontal) with 5% velocity anomaly between 10 and 80 km horizontal distance. We also performed synthetic tests (Text S6) to assess the resolvability of the FWI method for a thick or thin MTZ. These synthetic tests indicate that the FWI can recover a MTZ as thin as 0.5 km or as thick as 3.5 km between 10 and 80 km horizontal distance (Figure S11-S17). Therefore, we only interpret the velocity structures between 10 and 80 km horizontal distance.

3. Results

Crustal structure

The upper crust is characterized by low Vp but high vertical velocity gradients (Figures 3A,B,D and E), where the Vp increases rapidly from 3.0±0.1 km/s at the basement to 6.5 km/s at 1.8±0.2 km depth. However, the inverted velocity model reveals a heterogeneous lower crust, where alternate high-and-low-velocity layers are observed (Figures 3A,D and E). We used the contour of vertical velocity gradient of 0 s^{-1} to represent the boundaries between the high- and low-velocity layers (Figure 3B). The thickness of these layers varies from 300-400 m to ~1 km. The maximum velocity reduction within the low-velocity layers is ~500 m/s.

At the base of the model at 8.0-9.5 km depth, a positive high velocity gradient zone is observed (Figure 3B), separating the typical lower crustal velocity above with the mantle velocity below. We picked the depth of the top of this zone, marked by a vertical velocity gradient of 0 s^{-1}, and smoothed it over a horizontal distance of 8 km, which is interpreted as the base of the crust (red dashed curves in Figures 3A,B). This base of the crust shallows from a depth of ~9.5 km between 10 and 20 km distance to ~8.0 km between 45 and 55 km distance, and it lies between 8.2 and 8.5 km depth further north (Figure 3B). The mean velocity at the base of the crust is ~7.0±0.2 km/s, consistent with the global average velocity (7.1±0.1 km/s) at the base of crust formed at fast-spreading ridges (Christeson *et al.*, 2019).

The interpreted crustal base derived from the FWI is shallower than the tomographic Moho from Canales *et al.* (2003) along the entire profile (Figure 3A). The crustal thickness varies between 5.1 and 6.5 km (red curve in Figure 3C) with an average thickness of ~5.6 km, thinner than the average crustal thickness (~6.8 km) obtained from the traveltime tomography (Canales *et al.*, 2003), but close to that (~5.8 km) estimated from the MCS studies in the neighbouring region (Aghaei *et al.*, 2014). The crust is thicker south of the 30-40 km horizontal distance at ~9°36’-9°41’N than to the north, and the thickest crust is observed between 10 and 20 km horizontal distance at ~9°25’-9°30’N (red curve in Figure 3C), which is consistent with the tomography study (Canales *et al.*, 2003) (Figure S3B) and seismic reflection study (Aghaei *et al.*, 2014; Barth and Mutter, 1996). The thinnest crust is observed at 40-60 km horizontal distance at 9°41’-9°51’N, and the crust gradually thickens by ~500 m further north (red curve in Figure 3C).

Moho transition zone (MTZ)

FWI does not provide a sharp boundary for the Moho, but an increase in velocity over a certain depth range, which we define as the MTZ. The base of the crust with zero velocity gradient marks the top of the MTZ. We used two approaches to define the bottom of the MTZ: (I) 7.85 km/s velocity contour, the global average velocity at the top of the mantle (< 7.5 Myr) for crust formed at fast-spreading ridges (Christeson *et al.*, 2019) and (II) the base of the high velocity gradient zone. If we pick the depth of the 7.85 km/s velocity contour (purple dashed curves in Figures 3A,B) the thickness of the MTZ would be between 1.1 and 2.4 km (blue dashed curve in Figure 3C). If we take the base of the large positive velocity gradient zone as the bottom of the MTZ (purple solid curves in Figures 3A,B), the thickness of the MTZ would be between 1.6 and 3.0 km (blue solid curve in Figure 3C) where the average mantle velocity is ~7.97±0.13 km/s. In both cases, the MTZ is relatively thin south of the 30 km horizontal distance at 9°36'N (blue curves in Figure 3C). The thickness of the MTZ shows a negative correlation with the crustal thickness along the profile, i.e., where the MTZ is thick the crust is thin, and vice versa (Figure 3C).

4. Discussion and conclusion

Our results show (I) the presence of layered structures in the lower crust, (II) the crust is thin in the north and thick in the south whereas the MTZ is thick in the north and thin in the south and (III) there is an inverse correlation between the crustal thickness and the MTZ thickness.

Seismic reflection studies of the 9°N EPR have shown the presence of axial melt lens (AML) at 1.4-1.9 km depth in the mid-crust (Detrick *et al.*, 1987; Kent *et al.*, 1993) whereas tomographic studies indicate the presence of low velocity zone down to 6-7 km depth below the seafloor (Dunn, 2022; Dunn *et al.*, 2000), indicating the existence of partial melt. Furthermore, Marjanović *et al.* (2014) and Arnulf *et al.* (2014) show the presence of secondary melt sills within 1.65 km depth below the AML. Studies of the Oman ophiolite suggest that the melt can intrude and crystalize at different depths in the lower crust (Boudier *et al.*, 1996; Kelemen *et al.*, 1997). The observed alternate high-and-low-velocity layering in the lower crust could be due to melt of different compositions injected and crystallised at different depths within the lower crust (Figure 4). The gabbroic rocks drilled from the Hess Deep in the equatorial Pacific are mainly composed of olivine, clinopyroxene and plagioclase (Carlson and Jay Miller, 2004; Lissenberg *et al.*, 2013). A small increase (by 5%) of the olivine content can lead up to 600 m/s increase in Vp of the gabbroic rocks (Carlson and Jay Miller, 2004; Guo *et al.*, 2022). Therefore, the low-velocity layers within the lower crust could be formed by melt with relatively low olivine concentration while the high-velocity layers could represent olivine-rich gabbroic sills. This interpretation supports the 'sheeted sill' model (Boudier *et al.*, 1996; Kelemen *et al.*, 1997) where in-situ melt intrusion and crystallization form the lower crust. Moreover, the off-axis melt sills (Aghaei *et al.*, 2017; Canales *et al.*, 2012; Han *et al.*, 2014) are observed up to a distance of ~12 km from the ridge crest and could form gabbroic sills with different compositions from those formed at the ridge axis, contributing to the formation of a heterogeneous lower crust.

An early study using one-dimensional velocity analysis found that the MTZ at ~9º35'N EPR is ~1.7 km at 10 km off-axis distance (Vera *et al.*, 1990). Another MCS study from the intermediate-spreading Juan de Fuca Ridge observed that the MTZ could be up to 2.0 km thick (Nedimović *et al.*, 2005). These estimates fall in the ranges of MTZ thickness obtained using FWI, but our results provide a 2-D view continuous over 70 km distance along the profile and its relationship to crustal structure.

There are two possibilities for the above observations. The along-strike variations in the MTZ thickness could be due to the different thermal structures among third-order discontinuities. Thermal structure plays an important role in controlling the vertical depth of melt introduction and crystallization at fast-spreading ridges (Maclennan *et al.*, 2004). For a relatively hot ridge segment, melt will pool and crystalize at shallower depth in the lower crust with little melt accumulate within the MTZ. In contrast, for a relatively cold ridge segment, some melt could accumulate at deeper depths in the lower crust or at Moho depth, forming a thick MTZ. Presence of melt around Moho depth beneath the 9-10^{o}N EPR has been observed in the seafloor compliance (Crawford *et al.*, 1991). The along-strike variations in the MTZ thickness could also reflect changes in the efficiency of melt migration through the MTZ beneath the spreading centre. A thin MTZ would indicate a rapid percolation of melt from the upwelling mantle to the accreting crust. The formation of a thick MTZ could be due to less efficient melt extraction from mantle to crust leading to the accumulation and crystallization of a large amount of melt within the transition zone (Figure 4). Melt crystallization might occur in the thin MTZ as well.

These interpretations are supported by the negative correlation between the thicknesses of the crust and MTZ. A relatively thick MTZ underlying a relatively thin crust suggests that a significant part of melt was crystallized in the MTZ. However, the total cumulative thickness of the crust and MTZ does not vary much along the profile, albeit the total melt supply from the mantle to crust might be uniform along the entire ridge segment.

Based on the study of Oman ophiolite, Nicolas *et al.* (1996) found that the thin lower crust is generally associated with a thick MTZ while the thick lower crust is associated with a thin MTZ, indicating that there is an anti-correlation between the ophiolite's crustal and MTZ thicknesses, assuming the combined thickness of the extrusive basalt and sheeted dike is constant. The extensive presence of thick gabbro sills observed in the relatively thick MTZ in the Oman ophiolite demonstrate that a large amount of magma has ponded within the MTZ (Boudier and Nicolas, 1995), supporting our interpretation.

Along our profile, the change from a relatively thin to thick MTZ occurs over a short distance of ~10 km (Figure 3C), and a similar pattern has been observed in the Oman ophiolite where the transition from a thin to thick MTZ occurs over <5 km distance (Jousselin and Nicolas, 2000). The seismic reflection study at 9ºN EPR (Aghaei *et al.*, 2014) also found that the character of the Moho reflection varies over 3-4 km spatial distance. Given different lateral resolutions of these methods, these observations indicate that the thermal structure and/or melt migration efficiency through MTZ can vary quickly along the ridge axis at fast-spreading ridge. Laterally abrupt changes in the thermal structure and melt migration efficiency will influence ridge segmentation, possibly governing the distributions of third-order ridge discontinuities (Aghaei *et al.*, 2014).

The average crustal thickness estimated from MCS data is ~5.8 km in the 9ºN EPR region (Aghaei *et al.*, 2014). However, seismic refraction study in the neighbouring region suggests ~1 km thicker crust (Canales *et al.*, 2003). This indicates a discrepancy in the oceanic crustal thickness obtained using seismic refraction and reflection methods, though these study areas are not exactly the same. The Moho depths estimated from reflection and refraction studies appear to have good consistency at some regions close to subduction trenches in the Pacific Ocean (Ivandic *et al.*, 2008; Kodaira *et al.*, 2014). However, in these studies, the Moho depths estimated from OBS data show large uncertainties of the order of ~1 km. In contrast, FWI of wide-angle seismic data can provide precise velocity of the crust and upper mantle and constrain the thickness of the MTZ, reconciling the discrepancy between the seismic reflection and the refraction methods. Our results demonstrate that the FWI method is a powerful tool for understanding the structures of crust and MTZ and crustal accretion processes at MORs.

Figures

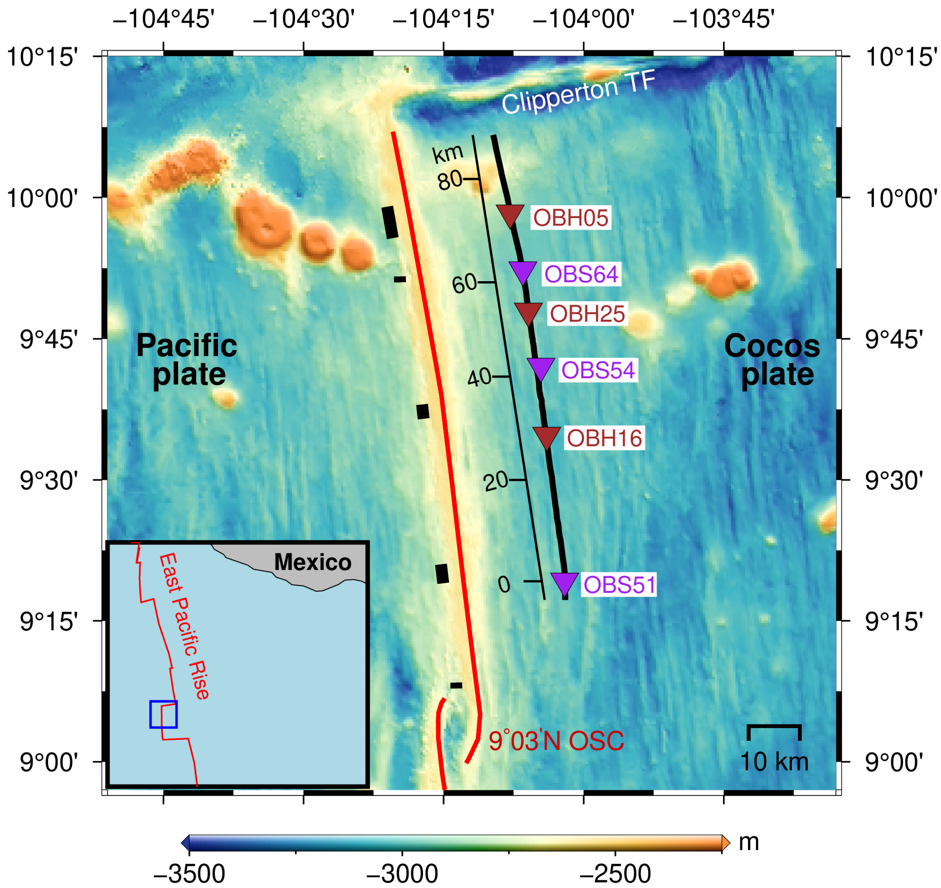

Figure 1. Bathymetry map of the study area. Red curves show the East Pacific Rise between the Clipperton transform fault (TF) and the 9°03'N overlapping spreading centre (OSC). The black rectangles show the locations of third-order discontinuities at 9°12'N, 9°20'N, 9°37'N, 9°51.5'N and 9°58'N from south to north, respectively (Aghaei *et al.*, 2014; White *et al.*, 2006). The black line indicates the seismic profile. Brown and purple triangles represent the locations of ocean bottom hydrophones (OBHs) and ocean bottom seismometers (OBSs), respectively. The blue box in the inset shows the location of the study area. The black scale shows the distance along the profile.

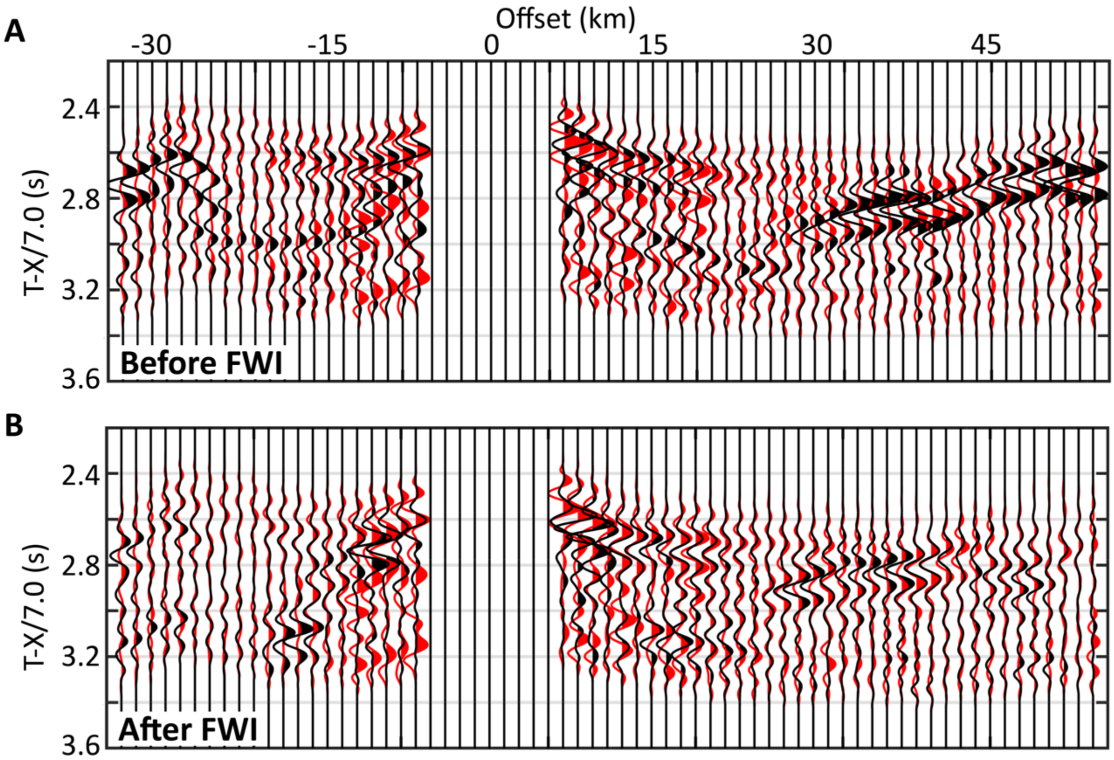

Figure 2. Comparisons of modelled and observed seismic data for OBH25. (A) Before FWI and (B) after FWI. The observed data is filtered to 3-10 Hz and the modelled data are calculated using the 3-10 Hz source wavelet. The modelled and observed seismic data are plotted in black and red, respectively. Traveltime (T) of the seismic data is reduced using a reduction velocity of 7.0 km/s. For better visibility, a scalar weighting factor ($1 + 0.1\times X$) was applied for each trace to enhance the amplitude at large offsets, where X is the offset.

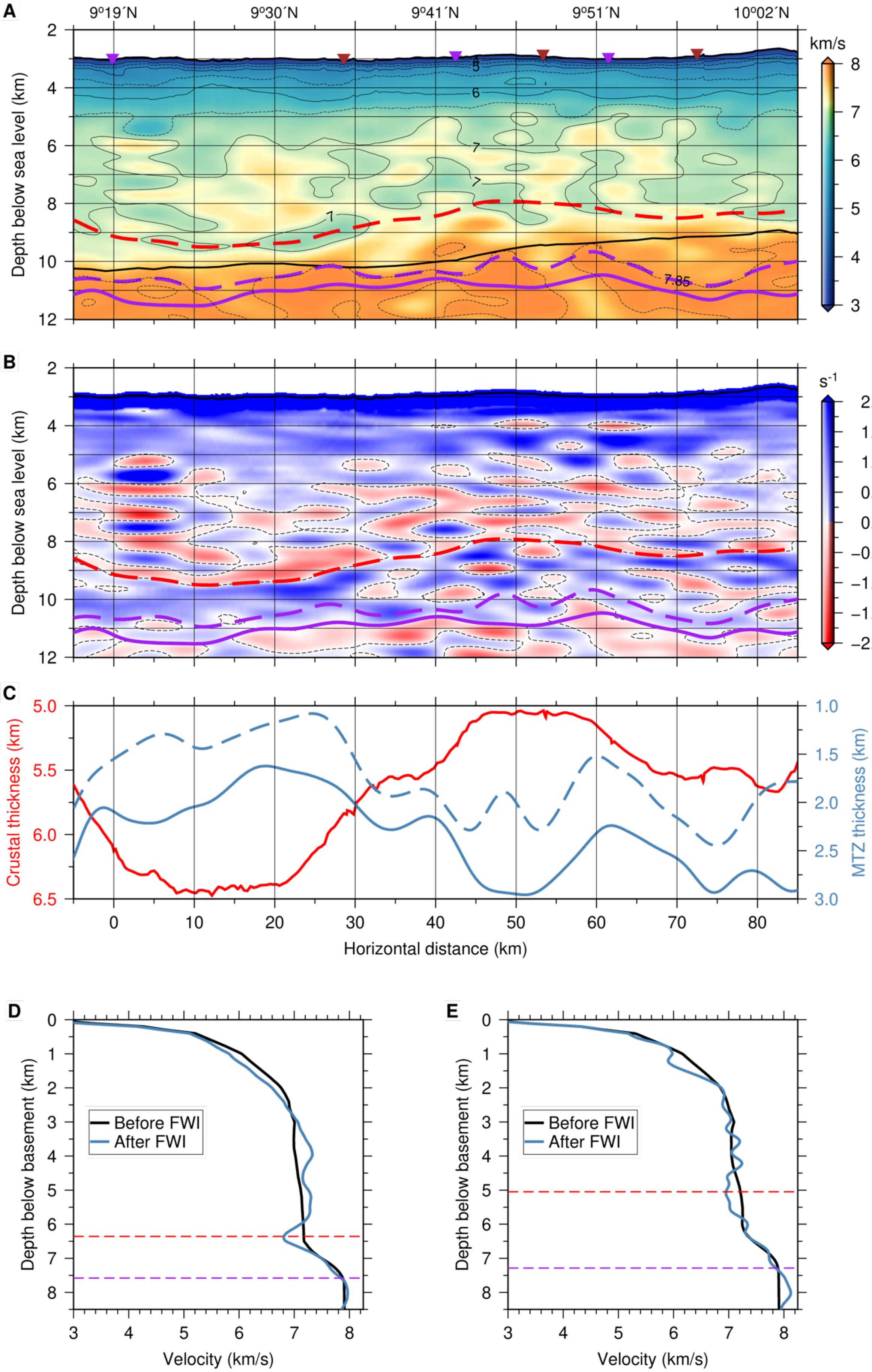
A
9º19´N
9º30´N
9º41´N
9º51´N
10º02´N
Depth below sea level (km)
km/s
7.85
B
s-1
C
Crustal thickness (km)
MTZ thickness (km)
Horizontal distance (km)
D
E
Depth below basement (km)
Before FWI
After FWI
Velocity (km/s)

323

Figure 3. Results of FWI. (A) Crustal and upper mantle P-wave velocity model from FWI. The thick black curve is the tomographic Moho from Canales *et al.* (2003). The red dashed curve is the interpreted crustal base corresponding to the top of the large positive velocity gradient zone beneath the crust. The dashed purple curve is the bottom of the MTZ interpreted using a smooth version of the 7.85 km/s velocity contour (Christeson *et al.*, 2019). The solid purple curve is the bottom of the MTZ interpreted using the base of the large positive velocity gradient zone. The 4.5, 5.5, 6.5 and 7.85 km/s velocity contours are shown as black dashed curves from top to bottom. The brown and purple triangles show the locations of OBHs and OBSs, respectively. (B) Vertical velocity gradient. The black dashed curves are the 0 s^{-1} velocity gradient contour. The red and the purple curves are the same as in A. (C) The crustal (in red) and the MTZ thickness (in blue) variations along the profile. The blue dashed and solid curves are the MTZ thickness calculated using a smooth version of the 7.85 km/s velocity contour (purple dashed curves in A,B) and using the base of the large positive velocity gradient zone (purple solid curves in A,B) as the bottom of the MTZ, respectively. (D) Comparison of the starting (in black) and final (in blue) inverted velocity profiles averaged between 16 and 24 km horizontal distance where the crust is thick and the MTZ is thin. (E) Comparison of the starting (in black) and final (in blue) inverted velocity profiles averaged between 46 and 54 km horizontal distance where the crust is thin and the MTZ is thick. The red and purple dashed lines in d and e represent the top of the MTZ and the MTZ bottom defined by 7.85 km/s velocity contour.

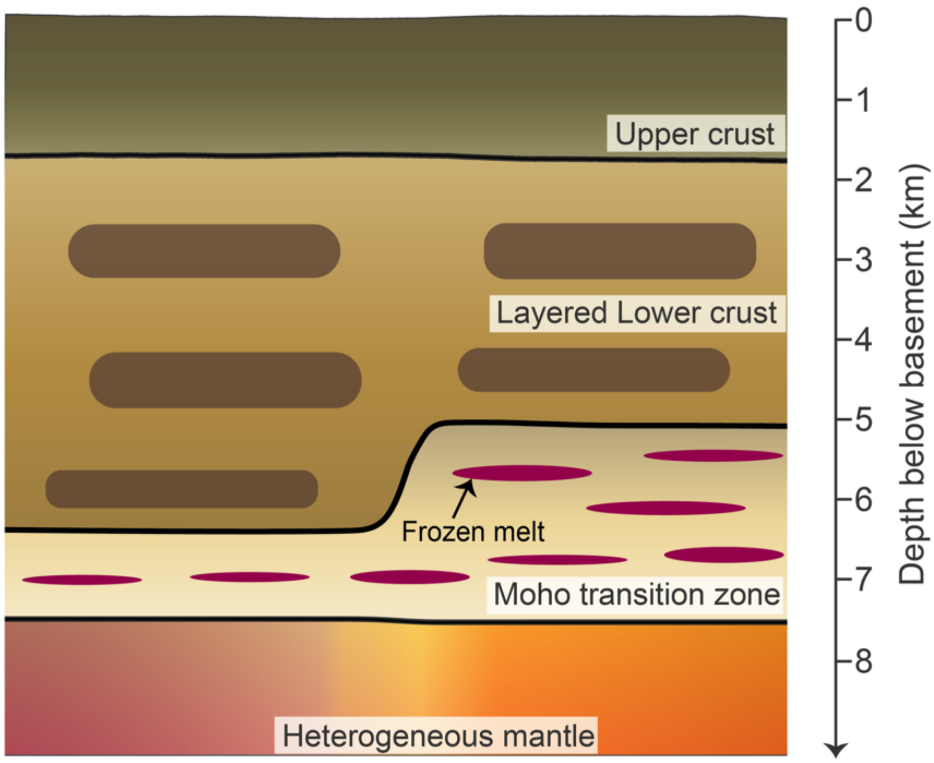

Figure 4. Schematic diagram showing structures of the oceanic crust and Moho transition zone (MTZ). The oceanic crust is separated into an upper crust (~1.8 km thick) and a layered lower crust. The dark brown blocks in the lower crust refer to the low-velocity layers from FWI. The layered lower crust indicates the oceanic lower crust is formed by in-situ melt injection and crystallization at different depths. The thickness of the MTZ varies along strike between 1.1 and 2.4 km, inversely correlated with the crustal thickness. The red horizontal elongated ellipsoids represent the frozen gabbro sills, which is accumulated and crystalized during its migration from the upwelling mantle to the crust.

REFERENCES

Aghaei, O., M. R. Nedimović, H. Carton, S. M. Carbotte, J. P. Canales, and J. C. Mutter (2014), Crustal thickness and Moho character of the fast-spreading East Pacific Rise from 9° 42′N to 9°57′N from poststack-migrated 3-D MCS data, *Geochem. Geophys. Geosyst.*, *15*(3), 634-657, doi:https://doi.org/10.1002/2013GC005069.

Aghaei, O., M. R. Nedimović, M. Marjanović, S. M. Carbotte, J. Pablo Canales, H. Carton, and N. Nikić (2017), Constraints on melt content of off-axis magma lenses at the East Pacific Rise from analysis of 3-D seismic amplitude variation with angle of incidence, *J. Geophys. Res.*, *122*(6), 4123-4142, doi:https://doi.org/10.1002/2016JB013785.

Arnulf, A. F., S. C. Singh, and J. W. Pye (2014), Seismic evidence of a complex multi-lens melt reservoir beneath the 9° N Overlapping Spreading Center at the East Pacific Rise, *Geophys. Res. Lett.*, *41*(17), 6109-6115, doi:https://doi.org/10.1002/2014GL060859.

Barth, G. A., and J. C. Mutter (1996), Variability in oceanic crustal thickness and structure: Multichannel seismic reflection results from the northern East Pacific Rise, *J. Geophys. Res.*, *101*(B8), 17951-17975, doi:https://doi.org/10.1029/96JB00814.

Benn, K., A. Nicolas, and I. Reuber (1988), Mantle—crust transition zone and origin of wehrlitic magmas: Evidence from the Oman ophiolite, *Tectonophysics*, *151*(1), 75-85, doi:https://doi.org/10.1016/0040-1951(88)90241-7.

Boudier, F., and A. Nicolas (1995), Nature of the Moho Transition Zone in the Oman Ophiolite, *J. Petrol.*, *36*(3), 777-796, doi:10.1093/petrology/36.3.777.

Boudier, F., A. Nicolas, and B. Ildefonse (1996), Magma chambers in the Oman ophiolite: fed from the top and the bottom, *Earth Planet. Sci. Lett.*, *144*(1), 239-250, doi:https://doi.org/10.1016/0012-821X(96)00167-7.

Brocher, T. M., J. A. Karson, and J. A. Collins (1985), Seismic stratigraphy of the oceanic Moho based on ophiolite models, *Geology*, *13*(1), 62-65, doi:10.1130/0091-7613(1985)13<62:Ssotom>2.0.Co;2.

Canales, J. P., H. Carton, S. M. Carbotte, J. C. Mutter, M. R. Nedimović, M. Xu, O. Aghaei, M. Marjanović, and K. Newman (2012), Network of off-axis melt bodies at the East Pacific Rise, *Nature Geosci.*, *5*(4), 279-283, doi:10.1038/ngeo1377.

Canales, P. J., R. S. Detrick, D. R. Toomey, and W. S. D. Wilcock (2003), Segment-scale variations in the crustal structure of 150–300 kyr old fast spreading oceanic crust (East Pacific Rise, 8°15′N–10°5′N) from wide-angle seismic refraction profiles, *Geophys. J. Int.*, *152*(3), 766-794, doi:10.1046/j.1365-246X.2003.01885.x.

Cann, J. R. (1970), New Model for the Structure of the Ocean Crust, *Nature*, *226*(5249), 928-930, doi:10.1038/226928a0.

Carlson, R. L., and D. Jay Miller (2004), Influence of pressure and mineralogy on seismic velocities in oceanic gabbros: Implications for the composition and state of the lower oceanic crust, *J. Geophys. Res.*, *109*(B9), B09205, doi:https://doi.org/10.1029/2003JB002699.

Christeson, G. L., J. A. Goff, and R. S. Reece (2019), Synthesis of Oceanic Crustal Structure From Two-Dimensional Seismic Profiles, *Rev. Geophys.*, *57*(2), 504-529, doi:https://doi.org/10.1029/2019RG000641.

Collins, J. A., T. M. Brocher, and J. A. Karson (1986), Two-dimensional seismic reflection modeling of the inferred fossil oceanic crust/mantle transition in the Bay of Islands Ophiolite, *J. Geophys. Res.*, *91*(B12), 12520-12538, doi:https://doi.org/10.1029/JB091iB12p12520.

Crawford, W. C., S. C. Webb, and J. A. Hildebrand (1991), Seafloor compliance observed by long-period pressure and displacement measurements, *J. Geophys. Res.*, *96*(B10), 16151-16160, doi:https://doi.org/10.1029/91JB01577.

Detrick, R. S., P. Buhl, E. Vera, J. Mutter, J. Orcutt, J. Madsen, and T. Brocher (1987), Multi-channel seismic imaging of a crustal magma chamber along the East Pacific Rise, *Nature*, *326*(6108), 35-41, doi:10.1038/326035a0.

Dunn, R. A. (2022), A Dual-Level Magmatic System Beneath the East Pacific Rise, 9°N, *Geophys. Res. Lett.*, *49*(18), e2022GL097732, doi:https://doi.org/10.1029/2022GL097732.

Dunn, R. A., D. R. Toomey, and S. C. Solomon (2000), Three-dimensional seismic structure and physical properties of the crust and shallow mantle beneath the East Pacific Rise at 9°30'N, *J. Geophys. Res.*, *105*(B10), 23537-23555, doi:https://doi.org/10.1029/2000JB900210.

Guo, P., S. C. Singh, V. Vaddineni, I. Grevemeyer, and E. Saygin (2022), Lower oceanic crust formed by in situ melt crystallization revealed by seismic layering, *Nature Geosci.*, *15*, 591–596, doi:https://doi.org/10.1038/s41561-022-00963-w.

Guo, P., S. C. Singh, V. A. Vaddineni, G. Visser, I. Grevemeyer, and E. Saygin (2020), Nonlinear full waveform inversion of wide-aperture OBS data for Moho structure using a trans-dimensional Bayesian method, *Geophys. J. Int.*, *224*(2), 1056-1078, doi:10.1093/gji/ggaa505.

Han, S., S. M. Carbotte, H. Carton, J. C. Mutter, O. Aghaei, M. R. Nedimović, and J. P. Canales (2014), Architecture of on- and off-axis magma bodies at EPR 9°37–40′N and implications for oceanic crustal accretion, *Earth Planet. Sci. Lett.*, *390*, 31-44, doi:https://doi.org/10.1016/j.epsl.2013.12.040.

Ivandic, M., I. Grevemeyer, A. Berhorst, E. R. Flueh, and K. McIntosh (2008), Impact of bending related faulting on the seismic properties of the incoming oceanic plate offshore of Nicaragua, *J. Geophys. Res.*, *113*(B5), doi:https://doi.org/10.1029/2007JB005291.

Jian, H., M. R. Nedimović, J. P. Canales, and K. W. H. Lau (2021), New Insights Into the Rift to Drift Transition Across the Northeastern Nova Scotian Margin From Wide-Angle Seismic Waveform Inversion and Reflection Imaging, *J. Geophys. Res.*, *126*(12), e2021JB022201, doi:https://doi.org/10.1029/2021JB022201.

Jousselin, D., and A. Nicolas (2000), The Moho transition zone in the Oman ophiolite-relation with wehrlites in the crust and dunites in the mantle, *Mar. Geophys. Res.*, *21*(3), 229-241, doi:10.1023/A:1026733019682.

Karson, J. A., J. A. Collins, and J. F. Casey (1984), Geologic and seismic velocity structure of the crust/mantle transition in the Bay of Islands Ophiolite Complex, *J. Geophys. Res.*, *89*(B7), 6126-6138, doi:https://doi.org/10.1029/JB089iB07p06126.

Kelemen, P. B., K. Koga, and N. Shimizu (1997), Geochemistry of gabbro sills in the crust-mantle transition zone of the Oman ophiolite: implications for the origin of the oceanic lower crust, *Earth Planet. Sci. Lett.*, *146*(3), 475-488, doi:https://doi.org/10.1016/S0012-821X(96)00235-X.

Kent, G. M., A. J. Harding, and J. A. Orcutt (1993), Distribution of magma beneath the East Pacific Rise between the Clipperton Transform and the 9°17′N Deval from forward modeling of common depth point data, *J. Geophys. Res.*, *98*(B8), 13945-13969, doi:https://doi.org/10.1029/93JB00705.

Kent, G. M., A. J. Harding, J. A. Orcutt, R. S. Detrick, J. C. Mutter, and P. Buhl (1994), Uniform accretion of oceanic crust south of the Garrett transform at 14°15′S on the East Pacific Rise, *J. Geophys. Res.*, *99*(B5), 9097-9116, doi:https://doi.org/10.1029/93JB02872.

Kodaira, S., G. Fujie, M. Yamashita, T. Sato, T. Takahashi, and N. Takahashi (2014), Seismological evidence of mantle flow driving plate motions at a palaeo-spreading centre, *Nature Geosci.*, *7*(5), 371-375, doi:10.1038/ngeo2121.

Levander, A. R. (1988), Fourth-order finite-difference P-SV seismograms, *Geophysics*, *53*(11), 1425-1436, doi:10.1190/1.1442422.

Lissenberg, C. J., C. J. MacLeod, K. A. Howard, and M. Godard (2013), Pervasive reactive melt migration through fast-spreading lower oceanic crust (Hess Deep, equatorial Pacific Ocean), *Earth Planet. Sci. Lett.*, *361*, 436-447, doi:https://doi.org/10.1016/j.epsl.2012.11.012.

Maclennan, J., T. Hulme, and S. C. Singh (2004), Thermal models of oceanic crustal accretion: Linking geophysical, geological and petrological observations, *Geochem. Geophys. Geosyst.*, *5*(2), doi:https://doi.org/10.1029/2003GC000605.

Marjanović, M., S. M. Carbotte, H. Carton, M. R. Nedimović, J. C. Mutter, and J. P. Canales (2014), A multi-sill magma plumbing system beneath the axis of the East Pacific Rise, *Nature Geosci.*, *7*(11), 825-829, doi:10.1038/ngeo2272.

Mutter, J. C., G. A. Barth, P. Buhl, R. S. Detrick, J. Orcutt, and A. Harding (1988), Magma distribution across ridge-axis discontinuities on the East Pacific Rise from multichannel seismic images, *Nature*, *336*(6195), 156-158, doi:10.1038/336156a0.

Nedimović, M. R., S. M. Carbotte, A. J. Harding, R. S. Detrick, J. P. Canales, J. B. Diebold, G. M. Kent, M. Tischer, and J. M. Babcock (2005), Frozen magma lenses below the oceanic crust, *Nature*, *436*(7054), 1149-1152, doi:10.1038/nature03944.

Nicolas, A., F. Boudier, and B. Ildefonse (1996), Variable crustal thickness in the Oman ophiolite: Implication for oceanic crust, *J. Geophys. Res.*, *101*(B8), 17941-17950, doi:https://doi.org/10.1029/96JB00195.

Pica, A., J. P. Diet, and A. Tarantola (1990), Nonlinear inversion of seismic reflection data in a laterally invariant medium, *Geophysics*, *55*(3), 284-292, doi:10.1190/1.1442836.

Shipp, R. M., and S. C. Singh (2002), Two-dimensional full wavefield inversion of wide-aperture marine seismic streamer data, *Geophys. J. Int.*, *151*(2), 325-344, doi:10.1046/j.1365-246X.2002.01645.x.

Tao, K., S. P. Grand, and F. Niu (2017), Full-waveform inversion of triplicated data using a normalized-correlation-coefficient-based misfit function, *Geophys. J. Int.*, *210*(3), 1517-1524, doi:10.1093/gji/ggx249.

Toomey, D. R., R. S. Detrick, and W. S. D. Wilcock (1997), Mapping melt and matrix flow in the uppermost mantle: undershooting the East Pacific Rise between the Siqueiros and Clipperton, R/V Maurice Ewing Leg 97–08, *Cruise Report, p. 163, Woods Hole Oceanogr. Inst., Woods Hole, MA.*

Vaddineni, V. A., S. C. Singh, I. Grevemeyer, P. Audhkhasi, and C. Papenberg (2021), Evolution of the Crustal and Upper Mantle Seismic Structure From 0–27 Ma in the Equatorial Atlantic Ocean at 2° 43′S, *J. Geophys. Res.*, *126*(6), e2020JB021390, doi:https://doi.org/10.1029/2020JB021390.

Vera, E. E., J. C. Mutter, P. Buhl, J. A. Orcutt, A. J. Harding, M. E. Kappus, R. S. Detrick, and T. M. Brocher (1990), The structure of 0- to 0.2-m.y.-old oceanic crust at 9°N on the East Pacific Rise from expanded spread profiles, *J. Geophys. Res.*, *95*(B10), 15529-15556, doi:doi:10.1029/JB095iB10p15529.

Virieux, J., and S. Operto (2009), An overview of full waveform inversion in exploration geophysics, *Geophysics*, *74*(6), WCC1–WCC26, doi:https://doi.org/10.1190/1.3238367.

Wang, Z., and S. C. Singh (2022), Seismic evidence for uniform crustal accretion along slow-spreading ridges in the equatorial Atlantic Ocean, *Nat. Commun.*, *13*(1), 7809, doi:10.1038/s41467-022-35459-z.

Wang, Z., S. C. Singh, and J. P. Canales (2024), Wide-angle seismic refraction data from the northern portion of the outer eastern profile, 9°N East Pacific Rise, *IPGP Research Collection*, url:https://dataverse.ipgp.fr/privateurl.xhtml?token=6eca5518-ffd6-4737-a016-32f5d28f5fea.

White, R. S., D. McKenzie, and R. K. O'Nions (1992), Oceanic crustal thickness from seismic measurements and rare earth element inversions, *J. Geophys. Res.*, *97*(B13), 19683-19715, doi:https://doi.org/10.1029/92JB01749.

White, S. M., R. M. Haymon, and S. Carbotte (2006), A new view of ridge segmentation and near-axis volcanism at the East Pacific Rise, 8°–12°N, from EM300 multibeam bathymetry, *Geochem. Geophys. Geosyst.*, *7*(12), doi:https://doi.org/10.1029/2006GC001407.

Acknowledgements

We thank the captain, crew and scientific team of the R/V Maurice Ewing Leg 97-08 for the data collection. Acquisition of the data used in this study was supported by NSF Award OCE-9634132. Z. Wang's contributions to this work were supported by the postdoctoral fellowship from the GPX project of Institut de Physique du Globe de Paris and partially by the Newton International Fellowships from the Royal Society. J.P. Canales' contributions to this study were supported by NSF Award OCE-0118383 and by the Independent Research & Development Program at WHOI. Results presented in this paper were performed either on the S-CAPAD platform of Institut de Physique du Globe de Paris or on the IRIDIS High Performance Computing Facility of the University of Southampton, and we acknowledge the associated support services in the completion of this work.

Author Contributions

Z.W. processed the data and wrote the paper. S.C.S. developed the project, supervised the data processing and wrote the paper. J.P.C. provided the tomographic velocity model. All authors discussed the results, participated in interpretation, and contributed to paper writing.

Competing Interests

The authors declare that they have no competing interests.

Open Research

The seismic data used in this study are available at the Institut de Physique du Globe de Paris (IPGP) Research Collection (Wang *et al.*, 2024).

Supporting Information for

Link between crustal thickness and Moho transition zone at 9ºN East Pacific Rise

Zhikai Wang[1,2], Satish C. Singh[1], and J. Pablo Canales[3]

[1] Institut de Physique du Globe de Paris, Université Paris Cité, 1 Rue Jussieu, 75005 Paris, France.

[2] Presently at School of Ocean and Earth Science, University of Southampton, European Way, SO14 3ZH Southampton, UK.

[3] Department of Geology and Geophysics, Woods Hole Oceanographic Institution, Woods Hole MA 02543, USA.

Contents of this file

Text S1. Finite-difference waveform modelling

The modelled seismic data are calculated by solving 2-D elastic wave equation using a temporal 2nd-order and spatial 4th-order staggered-grid finite-difference scheme [*Levander*, 1988]. To avoid numerical dispersion, we used 57.5 m and 28.75 m grid spacings, respectively, in the modelling of 3-5 Hz and 3-10 Hz data. These settings ensure five grid points are sampled by the shortest wavelength (wavelength in the water column), satisfying the dispersion condition [*Levander*, 1988]. Time steps of 4 ms and 2 ms were used in the modelling of 3-5 Hz and 3-10 Hz data, respectively, to keep the waveform modelling stable. An absorbing boundary condition [*Clayton and Engquist*, 1977] was used to attenuate the reflections from model boundaries.

Text S2. Source wavelet

An accurate source wavelet is critical for the success of FWI because the errors in seismic waveform difference due to an inaccurate source wavelet will be directly mapped into the velocity model. In this study, we estimated the source wavelet by stacking the near-offset water arrivals. The source wavelets are estimated separately for OBSs and OBHs. Here we detailed the workflow of source estimate for OBHs, and that for OBSs is the same except using OBS dataset. We extracted four near-offset traces from each OBH dataset after predictive gapped deconvolution and aligned these traces to the same starting time (0.05 s). The signals after 0.6 s were muted to mitigate the influence of seismic multiples and later reflections. These traces show high similarity in waveform of direct water arrivals (Figure S3A). We stacked the aligned traces (Figure S3B) and filtered the stacked signal (Figure S3C) using the same band-pass filters (3-5 Hz or 3-10 Hz) as applied to seismic data in FWI. The starting time of the source wavelet is determined by performing finite-difference waveform modelling and comparing the modelled and observed near-offset water wave. Figure S3C shows the source wavelets for OBSs (dashed curves) and OBHs (solid curves). Precise amplitude of the source wavelet is not needed because we normalized the seismic traces in the trace normalized FWI and the whole seismic gather in the true amplitude FWI (see text below). The good match between the modelled and observed near-offset direct water arrivals for OBH and OBS data (Figure S4) indicates that the estimated source wavelets are sufficiently accurate for performing FWI.

Text S3. Starting models

The water velocity is set to 1.5 km/s and is not updated in the FWI. The starting crustal P-wave velocity model is obtained from a ray-based travel time tomography of Pg and PmP arrivals

[*Canales et al.*, 2003]. The starting mantle P-wave velocity is expanded from a one-dimensional velocity profile hanging from the seafloor, where the mantle velocity increases linearly from 7.9 to 8.2 km/s within 5 km depth range. We smoothed the velocity around the tomographically constrained Moho to avoid a sharp boundary between the crust and mantle. The starting P-wave velocity model is shown in Figure S5. The starting S-wave velocity and density are calculated from P-wave velocity using the empirical relations given in [*Brocher*, 2005]. The S-wave velocity and density are not updated in the FWI.

Text S4. FWI

We used a 2-D time domain elastic FWI developed originally by *Shipp and Singh* [2002] for marine streamer data with constant shot and receiver spacings and modified the code to accommodate seismic data recorded by ocean bottom instruments with arbitrary geometry in 2-D space. Starting from an initial estimate of velocity of the subsurface, the elastic FWI iteratively updates the velocity model by reducing the misfit between the observed and modelled seismic data

$$m_{n+1} = m_n + \alpha_n g_n \, , \tag{1}$$

where m is the model parameter, α is a step length, g is the gradient of the misfit function [*Shipp and Singh*, 2002] and n is the iteration number. In this study, we only inverted the P-wave velocity of the subsurface. A constant step-length of 30 m/s was used in all iterations.

We simultaneously inverted the pressure data recorded by OBHs and the vertical component data of OBSs. The conventional elastic FWI directly compares the least-squared difference between the modelled and observed waveforms [*Shipp and Singh*, 2002; *Tarantola*, 1986]. Because the magnitude of amplitudes of the OBH and OBS data are very different, direct comparison of waveforms leads to unbalanced contributions to the gradient for OBH and OBS data. To solve this problem, two FWI approaches comparing normalised seismic data were used in this study.

We performed the trace normalized FWI of *Tao et al.* [2017] in the first stage. In this FWI approach, each trace of the observed and modelled data is normalised by its L_2-norm, and the misfit function is defined as the least-squared difference between the modelled and observed seismic data after trace-by-trace normalisation

$$J_1 = \sum_i^{N_s} \sum_j^{N_r} \left\| \frac{d_{i,j}}{\|d_{i,j}\|} - \frac{u_{i,j}}{\|u_{i,j}\|} \right\|^2, \tag{2}$$

where d and u represent the observed and modelled seismic data, N_s is the number of seismic gathers and N_r is the number of traces within each seismic gather, and $\| \quad \|$ represents the L$_2$ norm. From Equation (2), we can see that the trace normalised FWI is insensitive to the amplitude of the seismic data [*Tao et al.*, 2017]. Furthermore, the trace-normalised FWI is capable of inverting triplicated waveforms [*Tao et al.*, 2017], which in our case are the PmP arrivals. However, this method ignores the amplitude variation with offset (AVO) effect and mainly compares the phase information in seismic data, leading to reduced resolution than conventional FWI [*Liu et al.*, 2016]. The seismic residual of the trace normalised FWI is

$$R_{i,j} = \frac{1}{\|d_{i,j}\|\|u_{i,j}\|}\left(\frac{\int d_{i,j,t} \cdot u_{i,j,t} dt}{\|d_{i,j}\|\|u_{i,j}\|} u_{i,j} - d_{i,j}\right), \tag{3}$$

where $\int dt$ represents the integration over time and $\cdot$ is the multiplication operator.

To ensure the inversion convergence to the global minimum, we applied the multi-scale inversion strategy of *Bunks et al.* [1995] in the trace normalised FWI. We first inverted the seismic data between 3 and 5 Hz, and then this inverted velocity model was used as a starting model for the inversion of 3-10 Hz data. We also applied the multi-stage inversion strategy of *Shipp and Singh* [2002] for each frequency-band, where the near-offset (<20 km) data are inverted first and we increased the offset by 20 km every 7 iterations.

Taking the inverted model of the trace normalised FWI as starting model, we further performed 30 iterations of true amplitude FWI for 3-10 Hz data in the second stage. In the true amplitude, each seismic gather is normalised by the L$_2$-norm of the whole seismic gather, which scales the amplitude of OBH and OBS data to similar magnitude. The misfit function of the shot-normalised FWI is defined as the least-squared difference between the modelled and observed data after normalisation

$$J_2 = \sum_i^{N_s} \left\| \frac{d_i}{\|d_i\|} - \frac{u_i}{\|u_i\|} \right\|^2. \tag{4}$$

This FWI approach compares both the amplitude and the phase information, which can further refine the velocity of the subsurface. The seismic residual is defined as follows

$$r_{i,j} = \frac{1}{\|d_i\|\|u_i\|}\left(\frac{\int d_{i,j,t} \cdot u_{i,j,t} dtdr}{\|d_i\|\|u_i\|} u_{i,j} - d_{i,j}\right), \tag{5}$$

where $\int dtdr$ represents the integration over time and trace and j is the index of trace. The multi-offset inversion strategy of *Shipp and Singh* [2002] is not used in the second stage because no cycle skipping between modelled and observed data is observed after the trace-normalised FWI.

The gradient (g) in the FWI is computed by zero-lag cross-correlating the source generated forward-propagated wavefield and the adjoint source generated wavefield by back projecting the seismic residuals [*Shipp and Singh*, 2002]. We muted the gradient in the water column to avoid updating the velocity of water and we tapered the gradient within 115 m distance from OBHs and OBSs. A conjugate-gradient method [*Scales*, 1987] was used to speed up the convergence. The conjugate gradient was multiplied by square root of depth to partially account for spherical divergence [*Krebs et al.*, 2009], except for the last twenty iterations of the second stage where the conjugate gradient was multiplied by square of depth to further enhance the energy around and below the MTZ. To suppress the artifacts introduced by the sparse distribution of ocean bottom instruments, we applied a 2-D wavenumber domain low-passed filter [*Jian et al.*, 2021] to the velocity gradient. The low-passed filter is defined as

$$\left|\frac{k_x}{k_{cx}}\right| + \left|\frac{k_z}{k_{cz}}\right| = 1, \tag{6}$$

where k_x and k_z are the wavenumbers along horizontal distance and depth. k_{cx} and k_{cz} are the cut-off wavenumbers of the 2-D low-passed filter. k_{cx} is set as the inverse of the minimum distance (8 km) between two neighbouring ocean bottom instruments ($k_{cx} = 0.125\ \text{km}^{-1}$). We set k_{cz} as the maximum resolvable wavenumber ($k_{z\,max}$) of FWI, which is defined as follows [*Brenders and Pratt*, 2007]

$$k_{cz} = k_{z\,max} = \frac{2\pi f}{v}, \tag{7}$$

where f is the frequency and v is the background velocity. In this study, we used velocity $v =$ 6.5 km/s and the frequency f of 5 and 10 Hz to determine k_{cz} in FWI of 3-5 and 3-10 Hz data, respectively.

Text S5. Checkerboard test

We performed checkerboard tests to assess the resolution of the FWI result. The checkerboard input models are designed by adding 2-D sinusoidal anomalies into the crust and mantle of the FWI model. The maximum velocity perturbation is ±5%, which is the same as that used in the travel time tomography study from *Canales et al.* [2003]. We tested velocity anomalies with size of 0.5 × 10 km (horizontal × vertical), 0.5 × 8 km, 0.3 × 8 km and 0.5 × 5 km (Figure S7-10A). Synthetic seismic data are modelled by performing the finite-difference modelling using the estimated source wavelets of 3-10 Hz and the same source-receiver geometry as that of the field data. We inverted these synthetic seismic data using the same inversion parameters and time window as that for the FWI of the field data, starting from the final model of FWI using field data. We only performed the second stage of true amplitude FWI in the checkerboard tests, because no obvious cycle-skipping is observed. The results show that velocity anomalies of 0.5 × 10 km and 0.5 × 8 km size are completely recovered between 10 and 80 km horizontal distances (Figure S7B and S8B) and the velocity anomalies of 0.3 × 8 km size are recovered with locally reduced recovery in the mid-crust (Figure S9B). In contrast, the velocity anomalies of 0.5 × 5 km size are not recovered (Figure S10B). Therefore, the minimum resolution is ~8 km in the horizontal direction and ~0.3 km in the depth direction, and therefore, we only interpret anomalies larger than these values.

Text S6. Synthetic tests for the recovery of MTZ

We performed synthetic tests (Figure S11-S17) to assess the resolvability of the FWI method for a thick or thin MTZ, following the approach proposed in *Jian et al.* [2021]. A MTZ with velocity increasing linearly from 7.0 km/s to 7.85 km/s with depth is inserted in the final inverted model from FWI of OBS data. The thickness of MTZ is 0.5, 1.0, 1.5, 2.0, 2.5, 3.0 and 3.5 km in these tests (Figure S11-S17(A)), respectively. These designed models (hereafter referred to as 'synthetic true model') were used to generate synthetic seismic data by performing finite-difference modelling using the estimated source wavelets of 3-10 Hz and the same source-receiver geometry as that of the field data. We designed a starting model (Figure S11-S17(B)) for synthetic tests by smoothing the velocity below the top of the MTZ within the synthetic true model. The lateral width of the smoothing window is 8.0 km and the vertical width is twice of the thickness of the inserted MTZ. This is to ensure the starting model is smooth but doesn't lead to cycle-skipping. We only performed the inversion of 3-10 Hz data in the second stages of the FWI workflow. The same inversion parameters as those for FWI of field data were used in the synthetic tests. The final inverted models and comparisons of some 1-D velocity profiles are shown in Figure S11-S17(C). The difference between the synthetic true and starting models is shown in Figure S11-S17(D) and that between the synthetic true and inverted models is shown in Figure S11-S17(E). For the 0.5 km thick MTZ, the velocity of the MTZ is partially recovered between 10 and 80 km horizontal distance (Figure S11). In contrast, the velocity of the inserted MTZ between 10 and 80 km horizontal distance is almost completely recovered when the MTZ is 1.0-3.5 km thick (Figure S12-S17). The recovery of the MTZ at 10-25 km horizontal distance is slightly worse than that to the further north, likely due to sparser instruments deployed in this region.

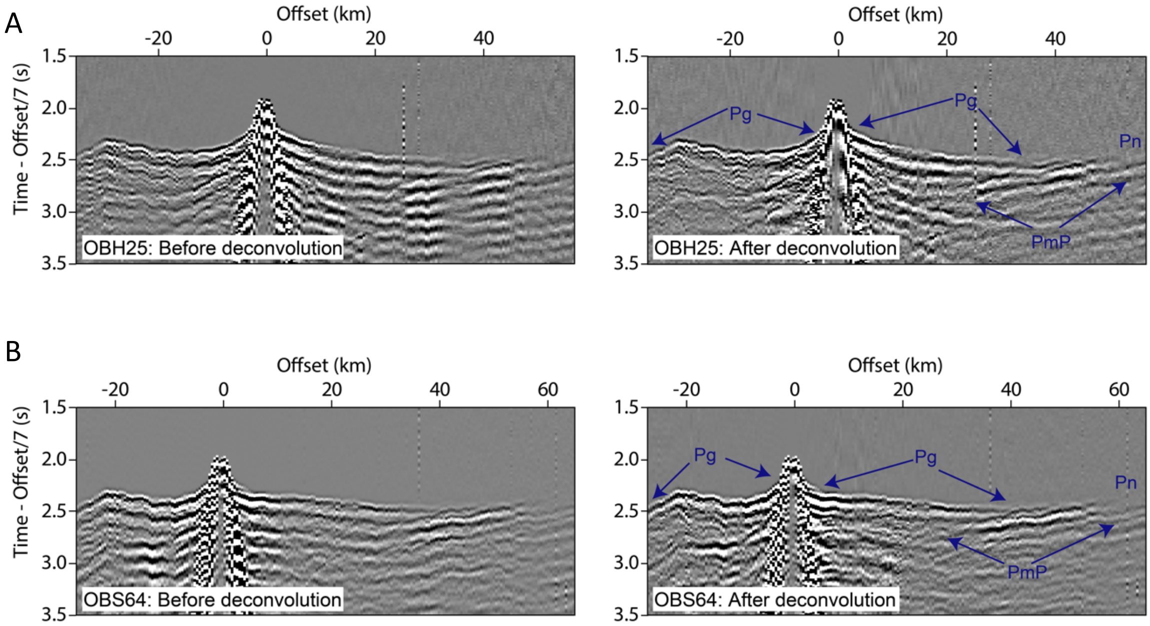

Figure S1. Comparisons of seismic data before (left column) and after (right column) predictive gapped deconvolution. (A) for OBH25 and (B) for OBS64. The travel time of seismic data is reduced using a reduction velocity of 7.0 km/s. The seismic bubble pulses are supressed after the predictive gapped deconvolution, and the crustal refractions (Pg), the Moho reflections (PmP) and the mantle refractions (Pn) are clearer.

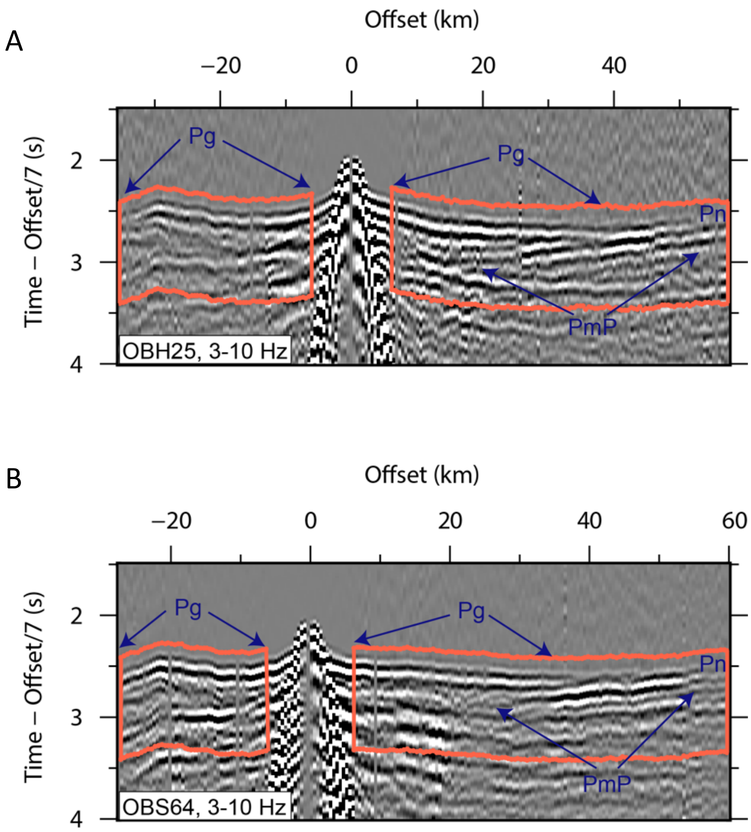

Figure S2. Time window overlapping on seismic plot. (A) for OBH25 and (B) for OBS64. The oranges boxes show the 1.0 s-wide time window used in the FWI of 3-10 Hz data. The waveforms of the Pg, PmP and Pn arrivals are included in the time window. The travel time of seismic data is reduced using a reduction velocity of 7.0 km/s.

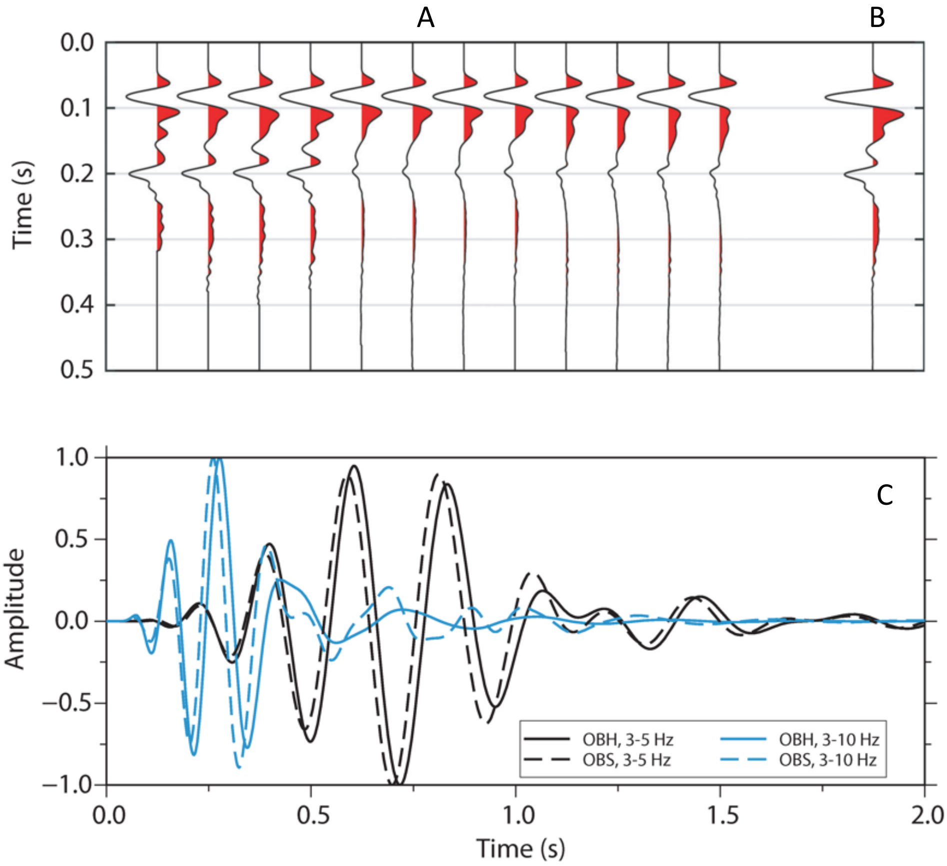

Figure S3. (A) Aligned seismic traces showing the near-offset direct water wave extracted from OBH gathers after filtering between 3-30 Hz. (B) Stack of traces in A. (C) The black and blue solid curves show the source wavelets for modelling of OBH data obtained by filtering the stacked signal in b to 3-5 Hz and 3-10 Hz, respectively. The black and blue dashed curves are the source wavelets for modelling of 3-5 and 3-10 Hz OBS data, respectively.

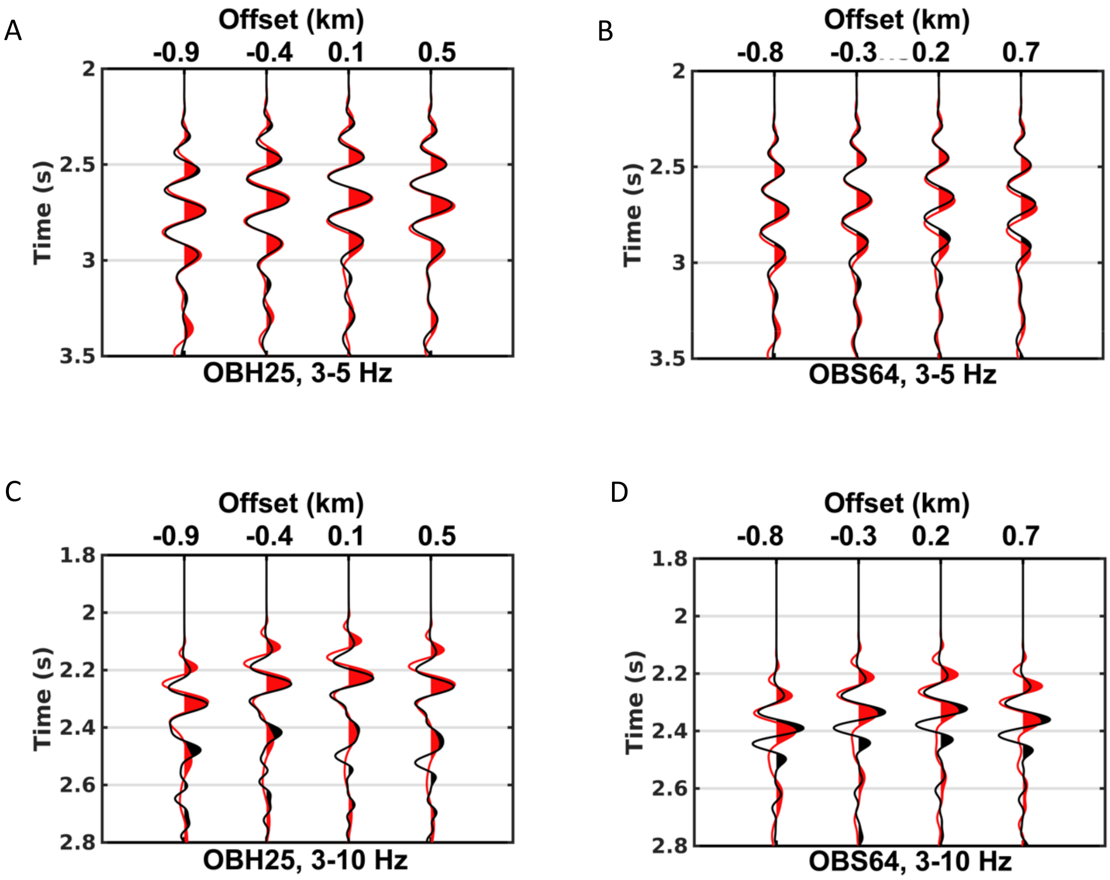

Figure S4. Comparisons of synthetic (in black) and observed (in red) near-offset water wave for OBH25 (A,C) and OBS64 (B,D). The synthetic data shown in A,B and C,D are modelled using the tomographic model using the 3-5 and 3-10 Hz source wavelets, respectively. The source wavelets are shown in Supplementary Fig. 4C. Correspondingly, the observed data are filtered to 3-5 Hz in A,B and to 3-10 Hz in C,D, respectively. The good match between the synthetic and observed data demonstrates the estimated source wavelets in Supplementary Fig. 4C are accurate enough for performing FWI.

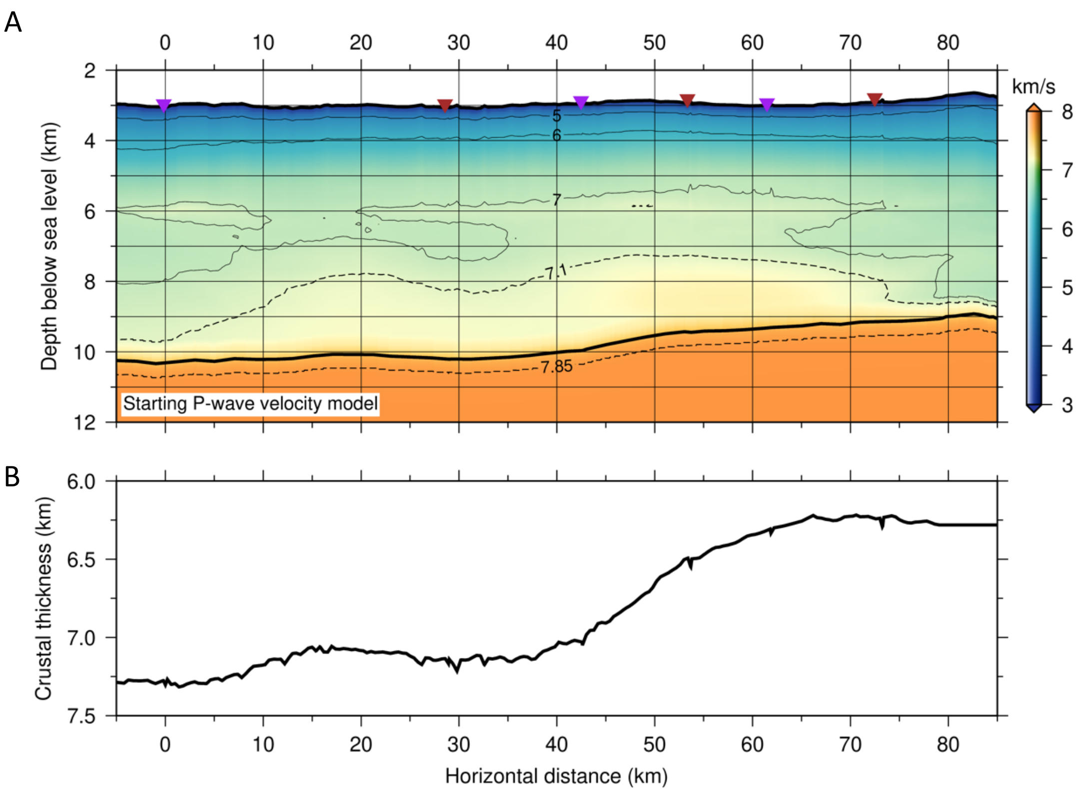

Figure S5. (A) Starting P-wave velocity model for FWI. The thick black curve is the tomographic Moho from *Canales et al.* [2003]. The brown and purple triangles show the locations of OBHs and OBSs, respectively. (B) Variation of crustal thickness obtained from travel time tomography [*Canales et al.*, 2003].

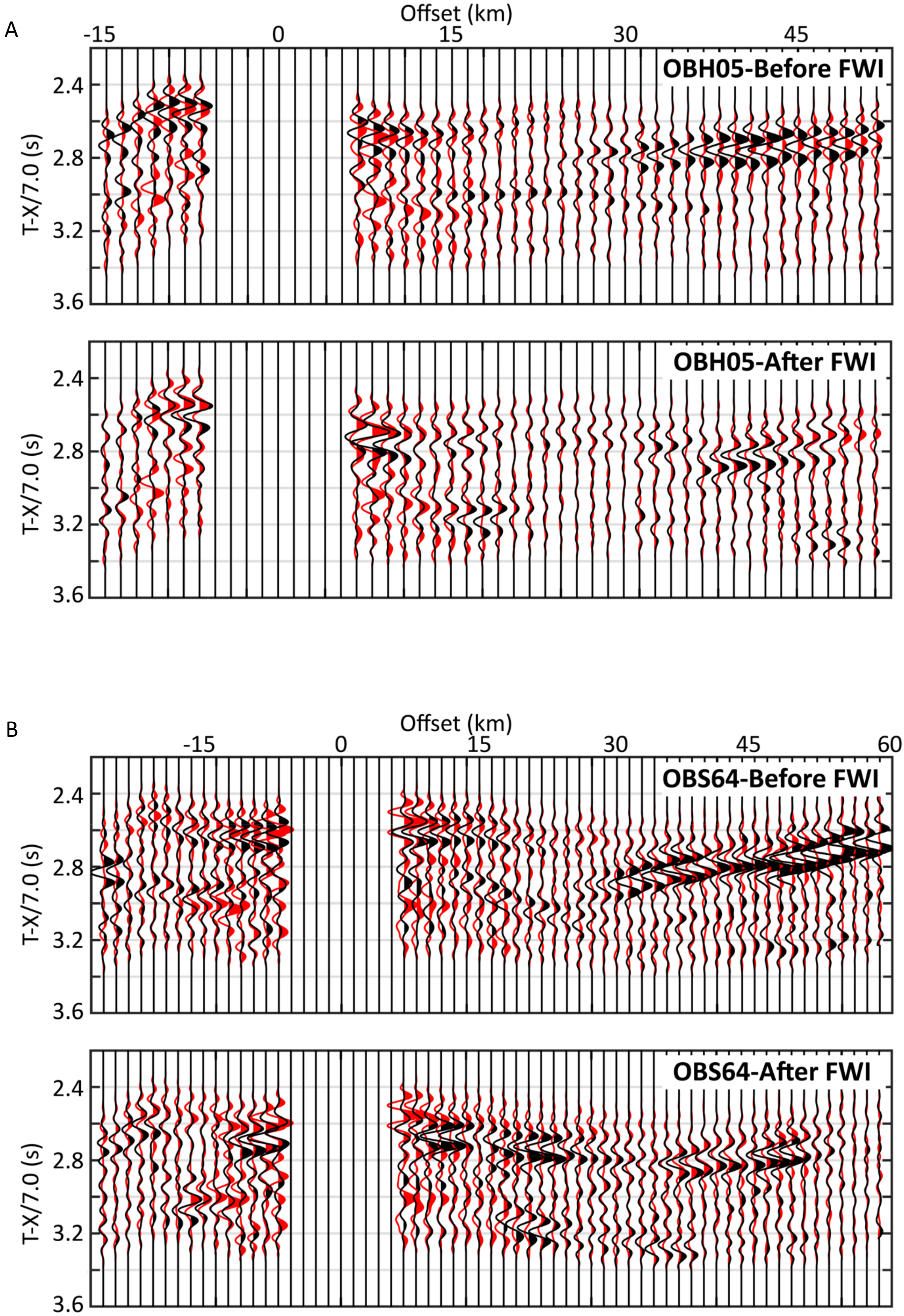
A
Offset (km)
-15
0
15
30
45
OBH05-Before FWI
OBH05-After FWI
T-X/7.0 (s)
2.4
2.8
3.2
3.6
B
Offset (km)
-15
0
15
30
45
60
OBS64-Before FWI
OBS64-After FWI
T-X/7.0 (s)
2.4
2.8
3.2
3.6

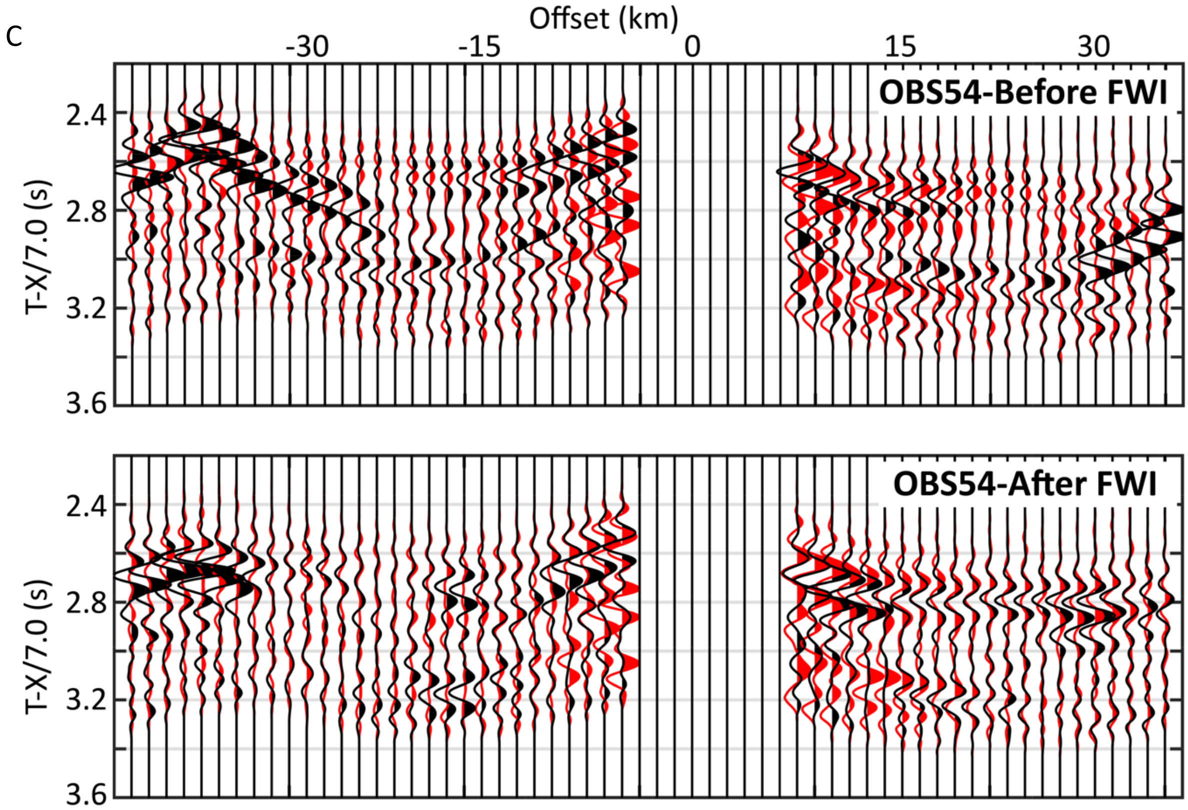
C
Offset (km)
-30
-15
0
15
30
OBS54-Before FWI
OBS54-After FWI
T-X/7.0 (s)
2.4
2.8
3.2
3.6

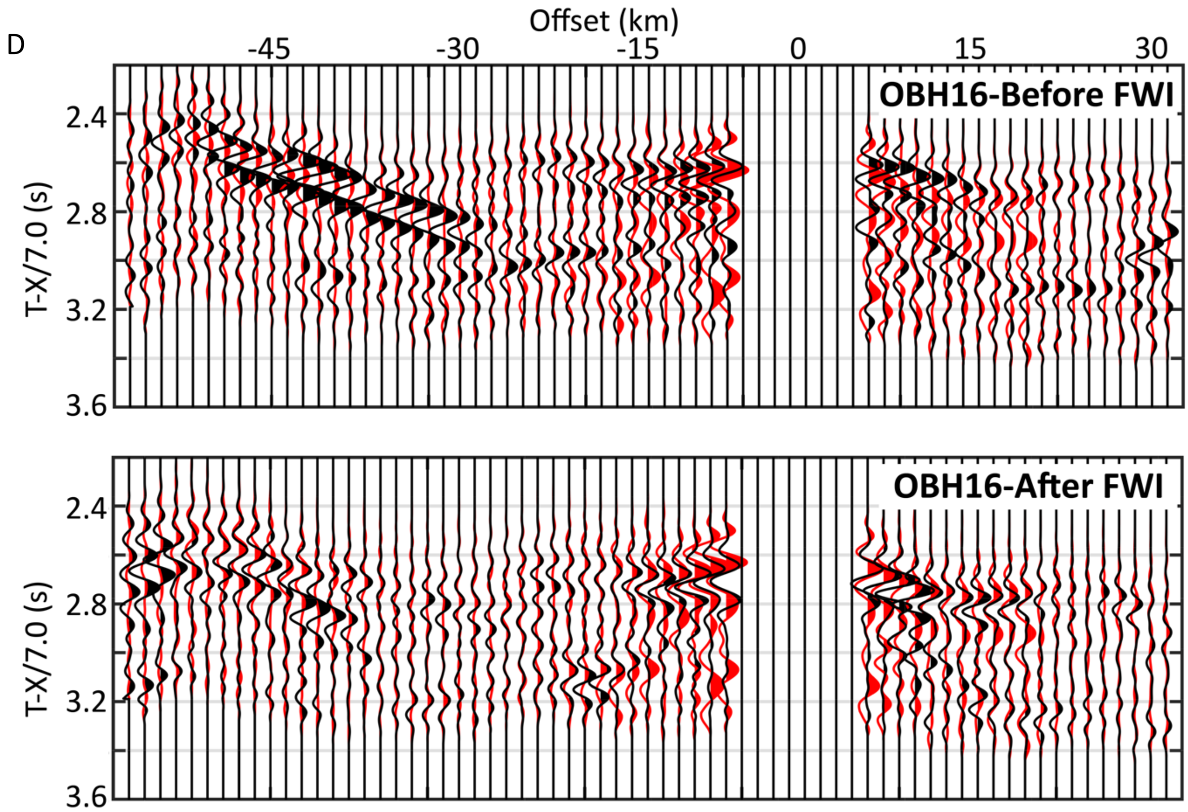
D
Offset (km)
-45
-30
-15
0
15
30
OBH16-Before FWI
OBH16-After FWI
T-X/7.0 (s)
2.4
2.8
3.2
3.6

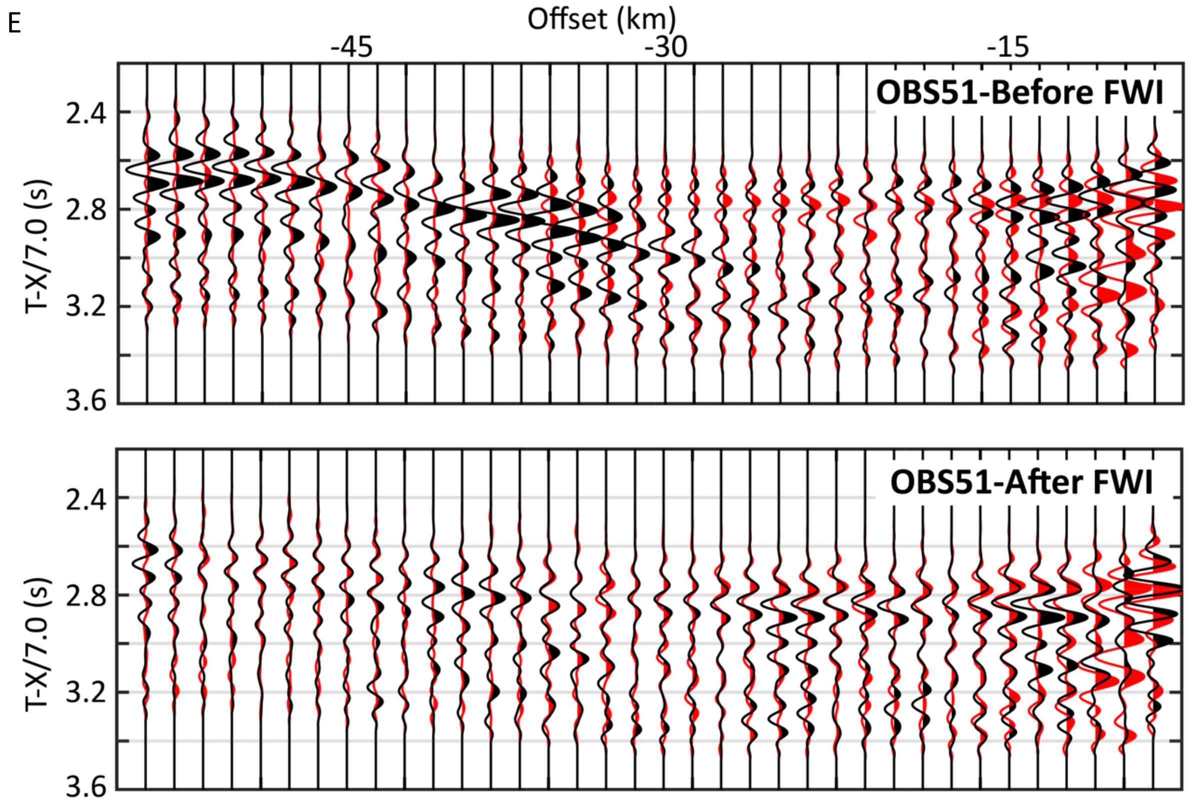

Figure S6. Comparisons of modelled (in black) and observed (in red) seismic data (3-10 Hz) before and after full waveform inversion (FWI). Travel time (T) of seismic data is reduced using a reduction velocity of 7.0 km/s. For better visibility, a scalar weighting factor (1+0.1×X) was multiplied for each trace to enhance the amplitude at large offsets, where X is offset. (A) OBH05; (B) OBS64; (C) OBS54; (D) OBH16; (E) OBS51.

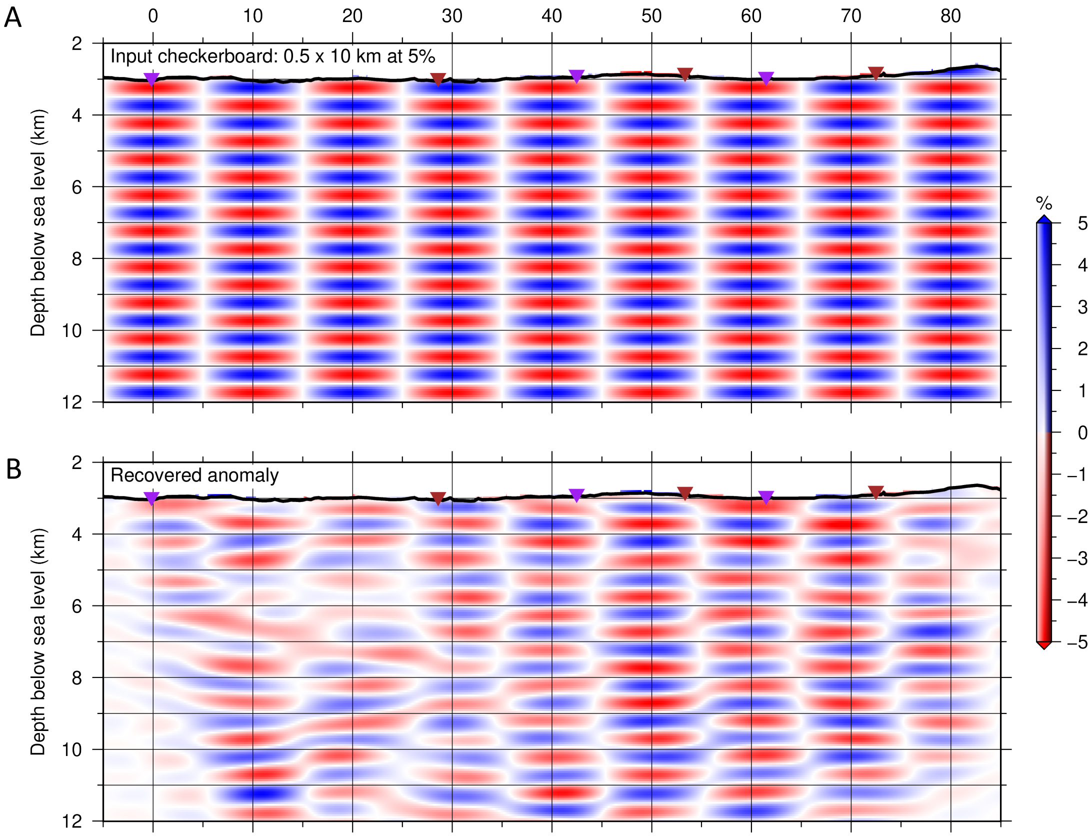

Figure S7. Checkerboard test using 0.5×10 km (vertical × horizontal) checkerboard pattern. Panels (A) and (B) show the input checkerboard pattern and the recovered anomaly, respectively. The maximum velocity perturbation is 5%. The brown and purple triangles show the locations of OBHs and OBSs, respectively.

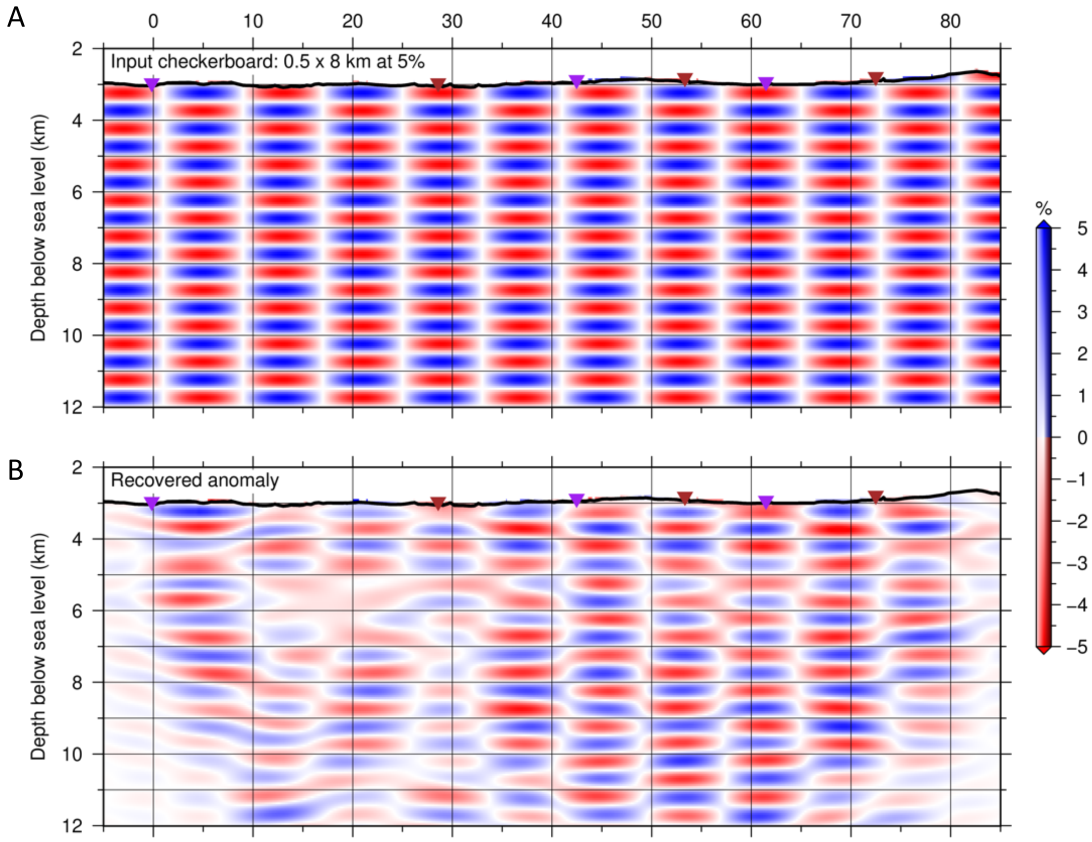

Figure S8. Checkerboard test using 0.5×8 km (vertical × horizontal) checkerboard pattern. Panels (A) and (B) show the input checkerboard pattern and the recovered anomaly, respectively. The maximum velocity perturbation is 5%. The brown and purple triangles show the locations of OBHs and OBSs, respectively.

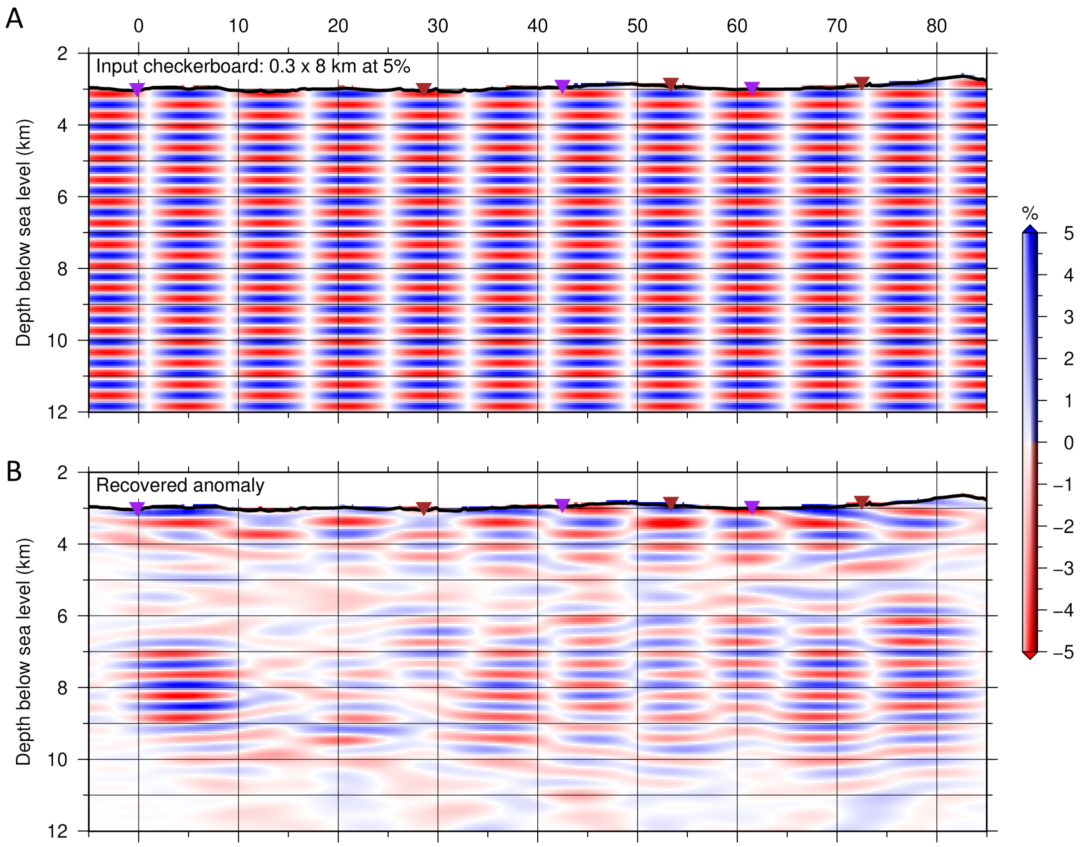

Figure S9. Checkerboard test using 0.3 × 8 km (vertical × horizontal) checkerboard pattern. Panels (A) and (B) show the input checkerboard pattern and the recovered anomaly, respectively. The maximum velocity perturbation is 5%. The brown and purple triangles show the locations of OBHs and OBSs, respectively.

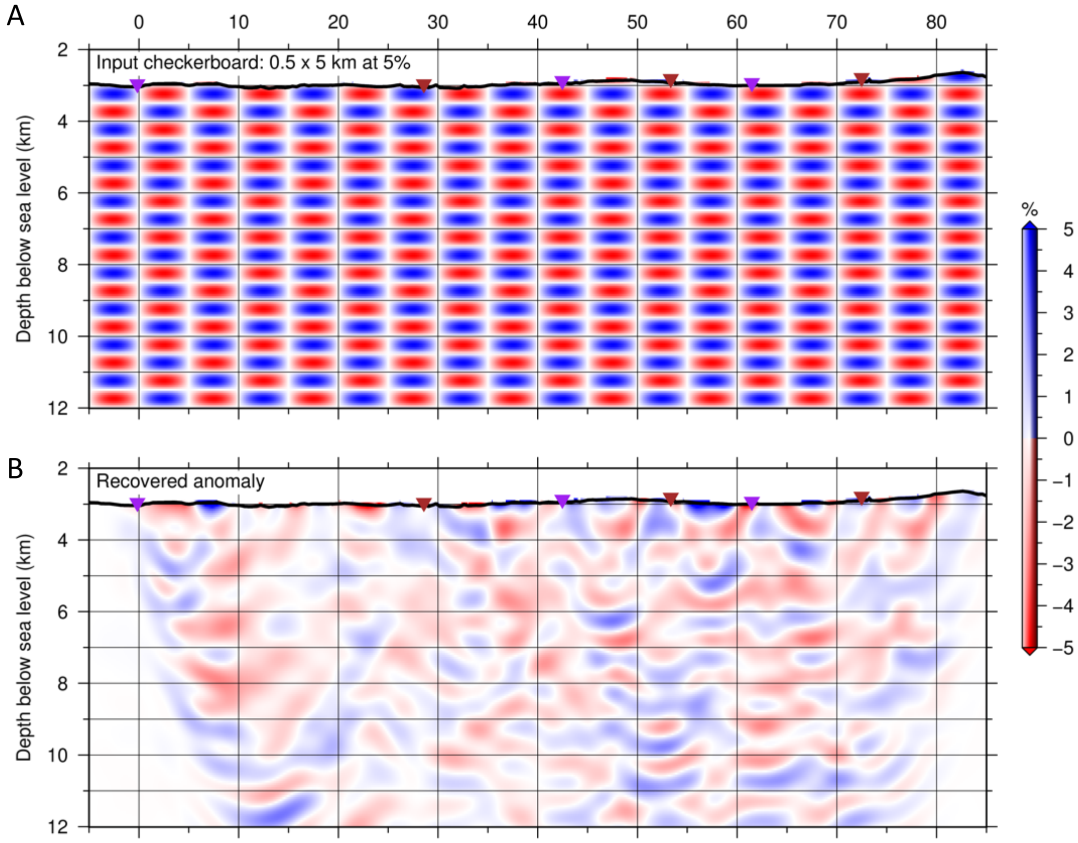

Figure S10. Checkerboard test using 0.5×5 km (vertical × horizontal) checkerboard pattern. Panels (A) and (B) show the input checkerboard pattern and the recovered anomaly, respectively. The maximum velocity perturbation is 5%. The brown and purple triangles show the locations of OBHs and OBSs, respectively.

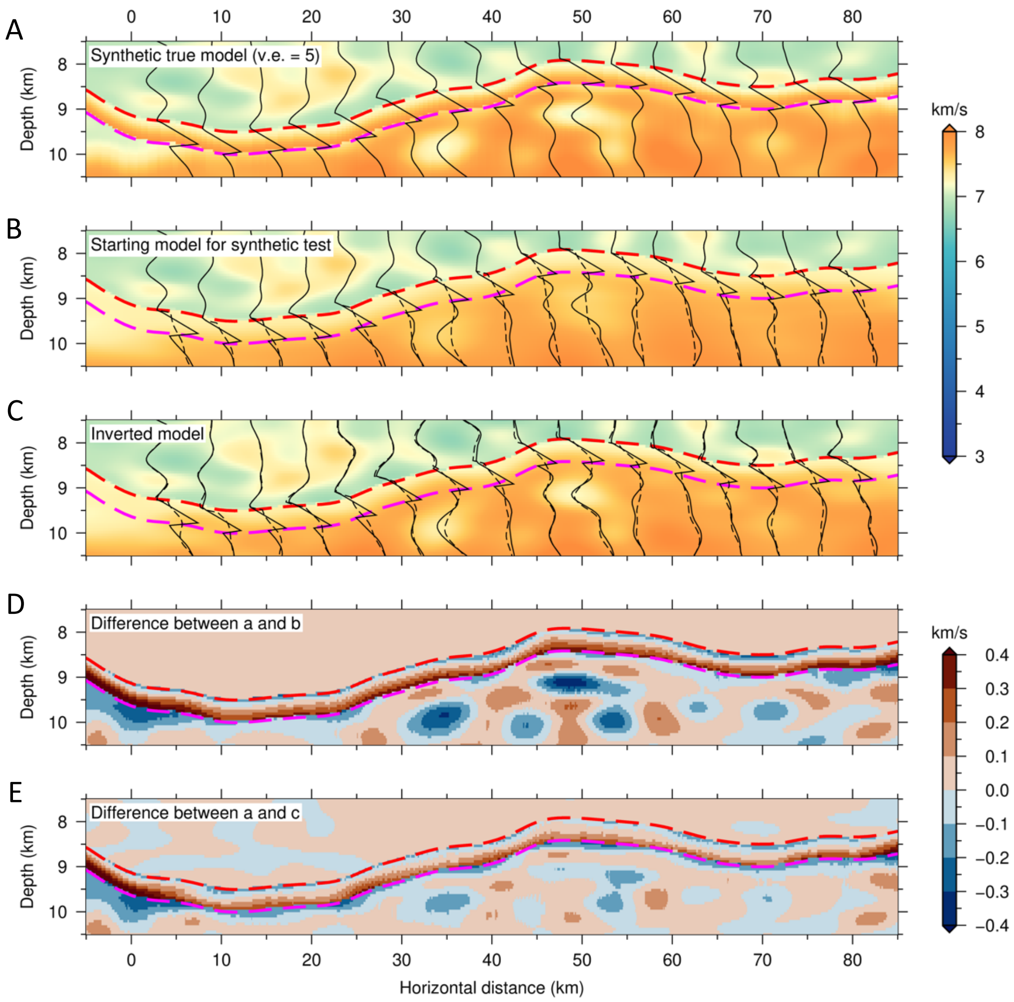

Figure S11. Synthetic test for the recovery of a 0.5 km thick Moho transition zone (MTZ). (A) True model for synthetic modelling which is modified by inserting a 0.5 km thick MTZ into the final model of full waveform inversion (FWI) of field data. Only the portion of the model around the MTZ is shown. The velocity of the inserted MTZ increases linearly with depth from 7.0 to 7.85 km/s. The 1-D profiles show vertical velocity profiles every 5 km between 5 and 80 km horizontal distance. (B) Starting model for synthetic test. The 1-D profiles compare the synthetic true (solid curves) and starting (dashed curves) velocities every 5 km between 5 and 80 km horizontal distance. (C) Inverted model from FWI. The 1-D profiles compare the synthetic true (solid curves) and inverted (dashed curves) velocities every 5 km between 5 and 80 km horizontal distance. (D) Difference between the synthetic true model (A) and the starting model (B). (E) Difference between the synthetic true model (A) and the inverted model (C). The red and magenta curves in A-E represent the top and bottom of the inserted 0.5 km thick MTZ, respectively.

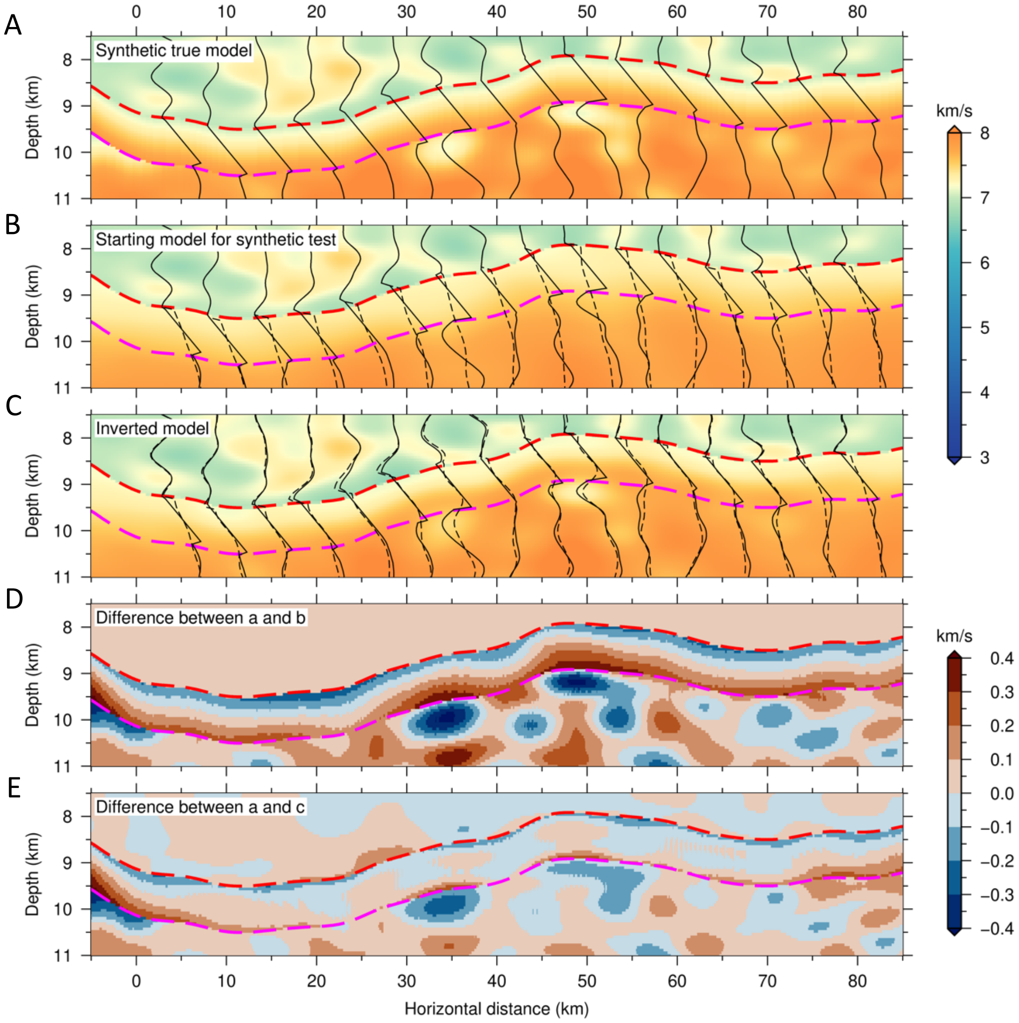

Figure S12. Synthetic test for the recovery of a 1.0 km thick Moho transition zone (MTZ). (A) True model for synthetic modelling which is modified by inserting a 1.0 km thick MTZ into the final model of full waveform inversion (FWI) of field data. Only the portion of the model around the MTZ is shown. The velocity of the inserted MTZ increases linearly with depth from 7.0 to 7.85 km/s. The 1-D profiles show vertical velocity profiles every 5 km between 5 and 80 km horizontal distance. (B) Starting model for synthetic test. The 1-D profiles compare the synthetic true (solid curves) and starting (dashed curves) velocities every 5 km between 5 and 80 km horizontal distance. (C) Inverted model from FWI. The 1-D profiles compare the synthetic true (solid curves) and inverted (dashed curves) velocities every 5 km between 5 and 80 km horizontal distance. (D) Difference between the synthetic true model (A) and the starting model (B). (E) Difference between the synthetic true model (A) and the inverted model (C). The red and magenta curves in A-E represent the top and bottom of the inserted 1.0 km thick MTZ, respectively.

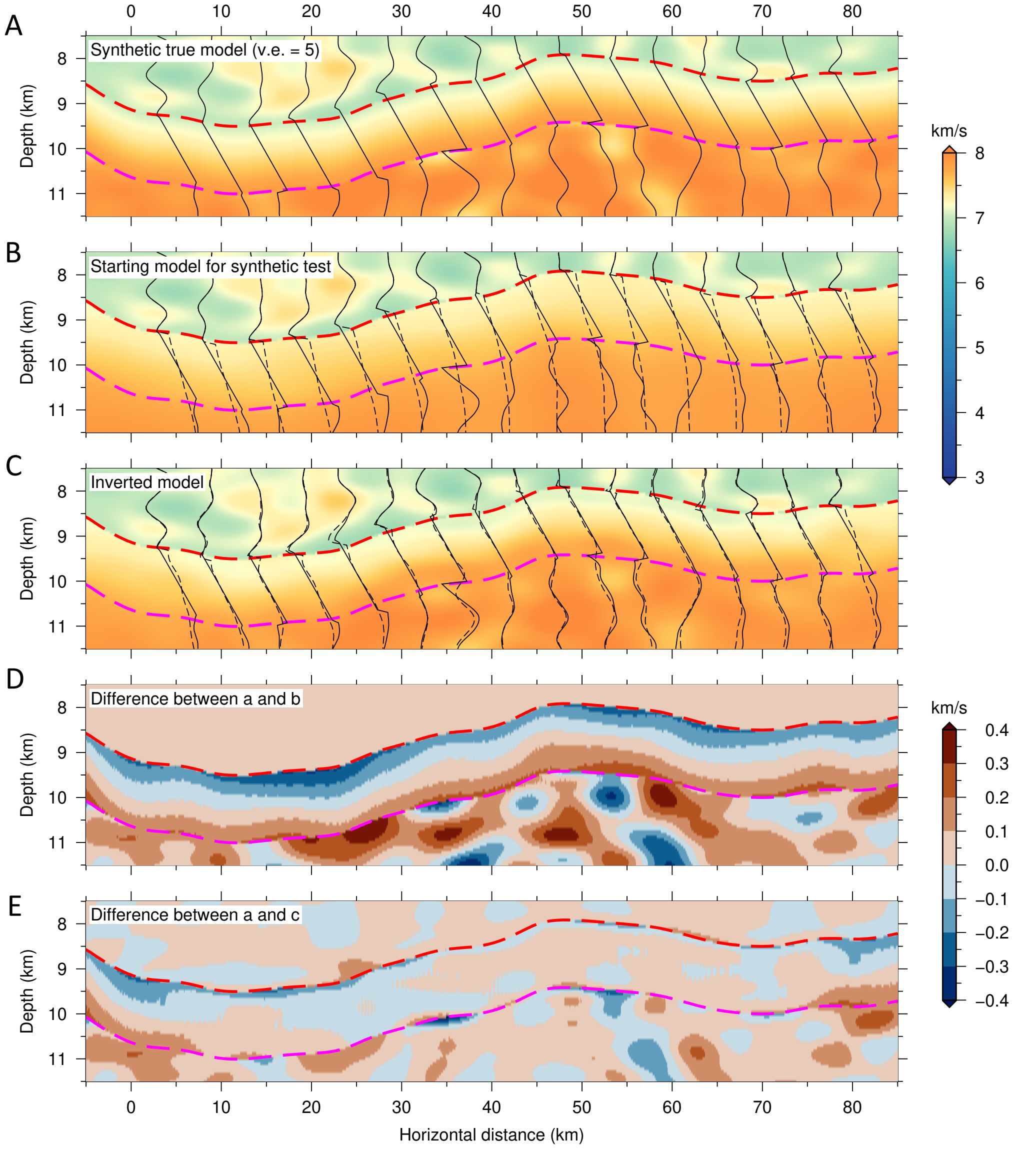

Figure S13. Synthetic test for the recovery of a 1.5 km thick Moho transition zone (MTZ). (A) True model for synthetic modelling which is modified by inserting a 1.5 km thick MTZ into the final model of full waveform inversion (FWI) of field data. Only the portion of the model around the MTZ is shown. The velocity of the inserted MTZ increases linearly with depth from 7.0 to 7.85 km/s. The 1-D profiles show vertical velocity profiles every 5 km between 5 and 80 km horizontal distance. (B) Starting model for synthetic test. The 1-D profiles compare the synthetic true (solid curves) and starting (dashed curves) velocities every 5 km between 5 and 80 km horizontal distance. (C) Inverted model from FWI. The 1-D profiles compare the synthetic true (solid curves) and inverted (dashed curves) velocities every 5 km between 5 and 80 km horizontal distance. (D) Difference between the synthetic true model (A) and the starting model (B). e: Difference between the synthetic true model (A) and the inverted model (C). The red and magenta curves in A-E represent the top and bottom of the inserted 1.5 km thick MTZ, respectively.

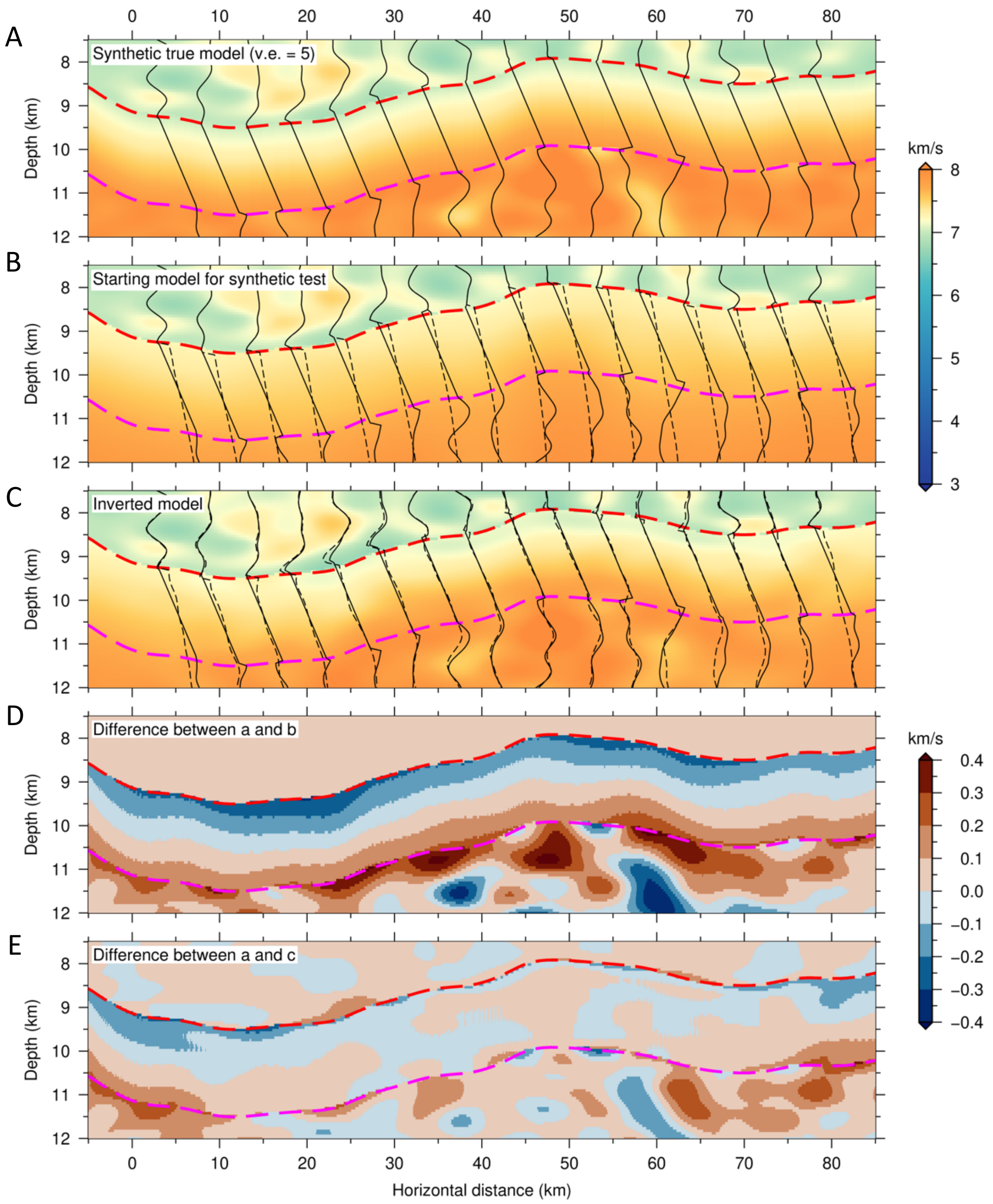

Figure S14. Synthetic test for the recovery of a 2.0 km thick Moho transition zone (MTZ). (A) True model for synthetic modelling which is modified by inserting a 2.0 km thick MTZ into the final model of full waveform inversion (FWI) of field data. Only the portion of the model around the MTZ is shown. The velocity of the inserted MTZ increases linearly with depth from 7.0 to 7.85 km/s. The 1-D profiles show vertical velocity profiles every 5 km between 5 and 80 km horizontal distance. (B) Starting model for synthetic test. The 1-D profiles compare the synthetic true (solid curves) and starting (dashed curves) velocities every 5 km between 5 and 80 km horizontal distance. (C) Inverted model from FWI. The 1-D profiles compare the synthetic true (solid curves) and inverted (dashed curves) velocities every 5 km between 5 and 80 km horizontal distance. (D) Difference between the synthetic true model (A) and the starting model (B). (E) Difference between the synthetic true model (A) and the inverted model (C). The red and magenta curves in A-E represent the top and bottom of the inserted 2.0 km thick MTZ, respectively.

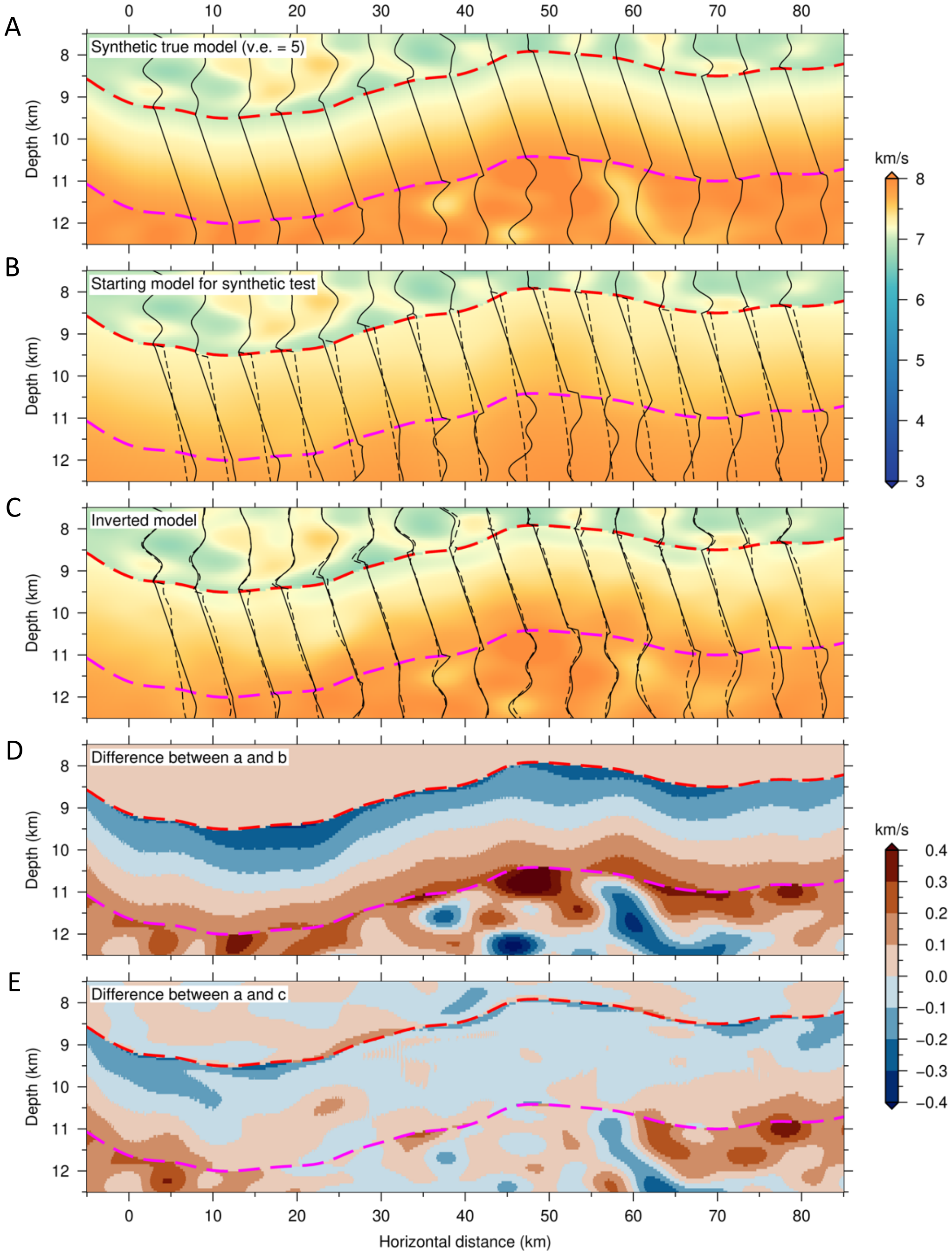

Figure S15. Synthetic test for the recovery of a 2.5 km thick Moho transition zone (MTZ). (A) True model for synthetic modelling which is modified by inserting a 2.5 km thick MTZ into the final model of full waveform inversion (FWI) of field data. Only the portion of the model around the MTZ is shown. The velocity of the inserted MTZ increases linearly with depth from 7.0 to 7.85 km/s. The 1-D profiles show vertical velocity profiles every 5 km between 5 and 80 km horizontal distance. (B) Starting model for synthetic test. The 1-D profiles compare the synthetic true (solid curves) and starting (dashed curves) velocities every 5 km between 5 and 80 km horizontal distance. (C) Inverted model from FWI. The 1-D profiles compare the synthetic true (solid curves) and inverted (dashed curves) velocities every 5 km between 5 and 80 km horizontal distance. (D) Difference between the synthetic true model (A) and the starting model (B). (E) Difference between the synthetic true model (A) and the inverted model (C). The red and magenta curves in A-E represent the top and bottom of the inserted 2.5 km thick MTZ, respectively.

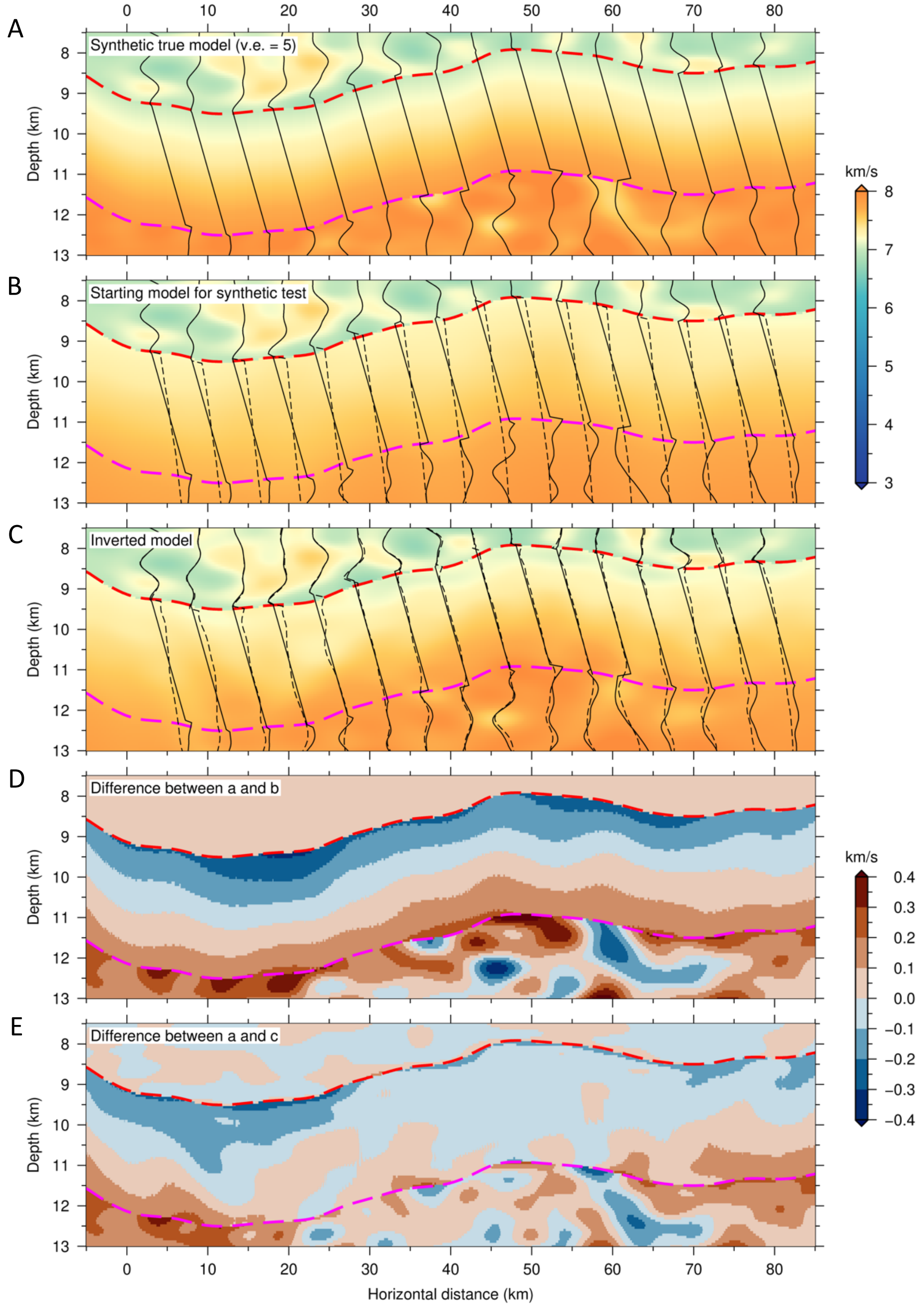

Figure S16: Synthetic test for the recovery of a 3.0 km thick Moho transition zone (MTZ). (A) True model for synthetic modelling which is modified by inserting a 3.0 km thick MTZ into the final model of full waveform inversion (FWI) of field data. Only the portion of the model around the MTZ is shown. The velocity of the inserted MTZ increases linearly with depth from 7.0 to 7.85 km/s. The 1-D profiles show vertical velocity profiles every 5 km between 5 and 80 km horizontal distance. (B) Starting model for synthetic test. The 1-D profiles compare the synthetic true (solid curves) and starting (dashed curves) velocities every 5 km between 5 and 80 km horizontal distance. (C) Inverted model from FWI. The 1-D profiles compare the synthetic true (solid curves) and inverted (dashed curves) velocities every 5 km between 5 and 80 km horizontal distance. (D) Difference between the synthetic true model (A) and the starting model (B). (E) Difference between the synthetic true model (A) and the inverted model (C). The red and magenta curves in A-E represent the top and bottom of the inserted 3.0 km thick MTZ, respectively.

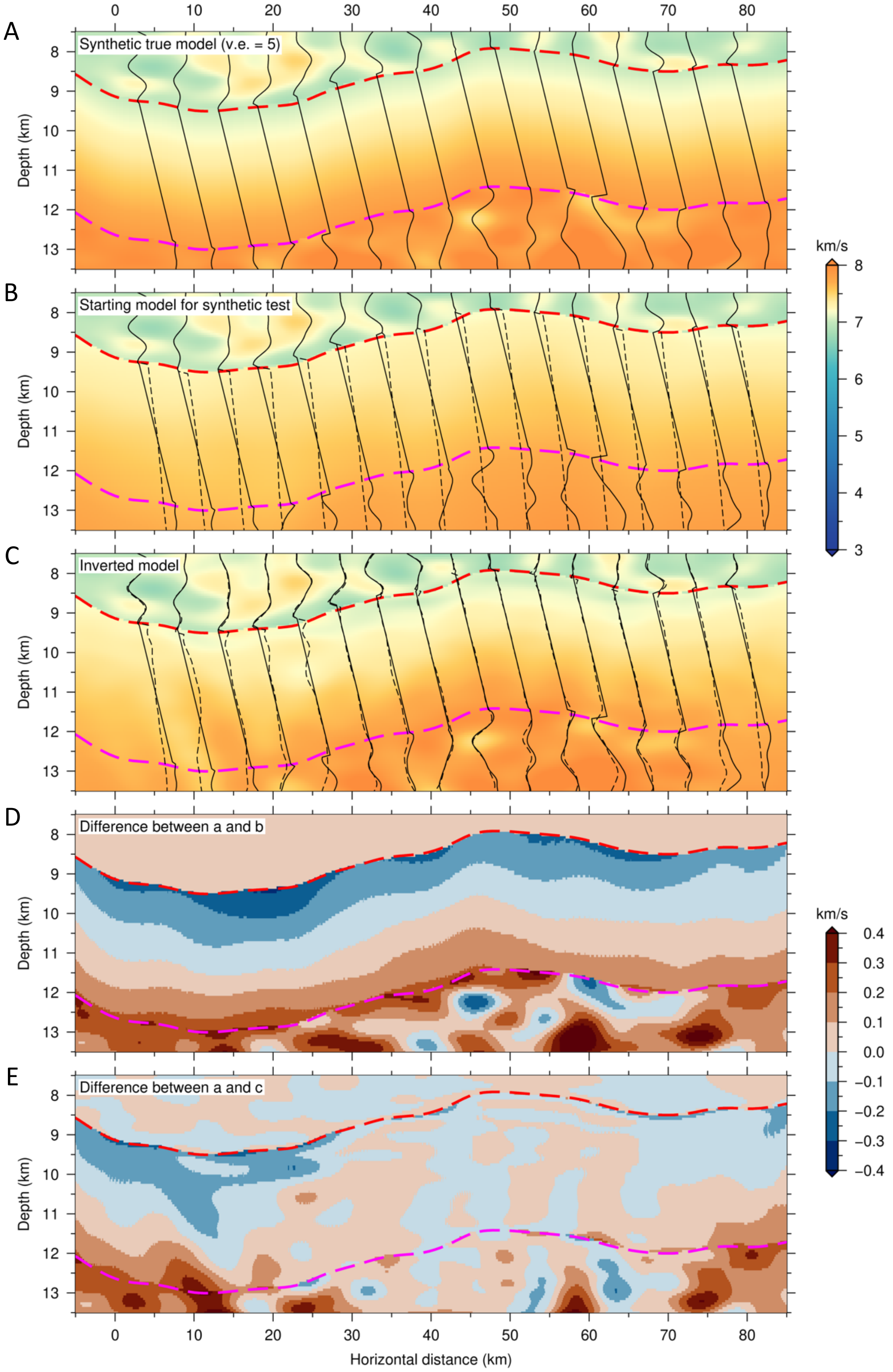

Figure S17. Synthetic test for the recovery of a 3.5 km thick Moho transition zone (MTZ). (A) True model for synthetic modelling which is modified by inserting a 3.5 km thick MTZ into the final model of full waveform inversion (FWI) of field data. Only the portion of the model around the MTZ is shown. The velocity of the inserted MTZ increases linearly with depth from 7.0 to 7.85 km/s. The 1-D profiles show vertical velocity profiles every 5 km between 5 and 80 km horizontal distance. (B) Starting model for synthetic test. The 1-D profiles compare the synthetic true (solid curves) and starting (dashed curves) velocities every 5 km between 5 and 80 km horizontal distance. (C) Inverted model from FWI. The 1-D profiles compare the synthetic true (solid curves) and inverted (dashed curves) velocities every 5 km between 5 and 80 km horizontal distance. (D) Difference between the synthetic true model (A) and the starting model (B). (E) Difference between the synthetic true model (A) and the inverted model (C). The red and magenta curves in a-e represent the top and bottom of the inserted 3.5 km thick MTZ, respectively.

References

Brenders, A. J., and R. G. Pratt (2007), Efficient waveform tomography for lithospheric imaging: implications for realistic, two-dimensional acquisition geometries and low-frequency data, *Geophys. J. Int.*, *168*(1), 152-170, doi:10.1111/j.1365-246X.2006.03096.x.

Brocher, T. M. (2005), Empirical Relations between Elastic Wavespeeds and Density in the Earth's Crust, *Bull. Seismol. Soc. Am.*, *95*(6), 2081-2092, doi:10.1785/0120050077.

Bunks, C., F. M. Saleck, S. Zaleski, and G. Chavent (1995), Multiscale seismic waveform inversion, *Geophysics*, *60*(5), 1457-1473, doi:doi:10.1190/1.1443880.

Canales, P. J., R. S. Detrick, D. R. Toomey, and W. S. D. Wilcock (2003), Segment-scale variations in the crustal structure of 150–300 kyr old fast spreading oceanic crust (East Pacific Rise, 8°15′N–10°5′N) from wide-angle seismic refraction profiles, *Geophys. J. Int.*, *152*(3), 766-794, doi:10.1046/j.1365-246X.2003.01885.x.

Clayton, R., and B. Engquist (1977), Absorbing boundary conditions for acoustic and elastic wave equations, *Bull. Seismol. Soc. Am.*, *67*(6), 1529-1540.

Jian, H., M. R. Nedimović, J. P. Canales, and K. W. H. Lau (2021), New Insights Into the Rift to Drift Transition Across the Northeastern Nova Scotian Margin From Wide-Angle Seismic Waveform Inversion and Reflection Imaging, *J. Geophys. Res.*, *126*(12), e2021JB022201, doi:https://doi.org/10.1029/2021JB022201.

Krebs, J. R., J. E. Anderson, D. Hinkley, R. Neelamani, S. Lee, A. Baumstein, and M.-D. Lacasse (2009), Fast full-wavefield seismic inversion using encoded sources, *Geophysics*, *74*(6), WCC177-WCC188, doi:doi:10.1190/1.3230502.

Levander, A. R. (1988), Fourth-order finite-difference P-SV seismograms, *Geophysics*, *53*(11), 1425-1436, doi:10.1190/1.1442422.

Liu, Y., J. Teng, T. Xu, Y. Wang, Q. Liu, and J. Badal (2016), Robust time-domain full waveform inversion with normalized zero-lag cross-correlation objective function, *Geophys. J. Int.*, *209*(1), 106–122, doi:10.1093/gji/ggw485.

Scales, J. A. (1987), Tomographic inversion via the conjugate gradient method, *Geophysics*, *52*(2), 179-185, doi:10.1190/1.1442293.

Shipp, R. M., and S. C. Singh (2002), Two-dimensional full wavefield inversion of wide-aperture marine seismic streamer data, *Geophys. J. Int.*, *151*(2), 325-344, doi:10.1046/j.1365-246X.2002.01645.x.

Tao, K., S. P. Grand, and F. Niu (2017), Full-waveform inversion of triplicated data using a normalized-correlation-coefficient-based misfit function, *Geophys. J. Int.*, *210*(3), 1517-1524, doi:10.1093/gji/ggx249.

Tarantola, A. (1986), A strategy for nonlinear elastic inversion of seismic reflection data, *Geophysics*, *51*(10), 1893-1903, doi:10.1190/1.1442046.